



# **Tectonics**°

## RESEARCH ARTICLE

10.1029/2021TC007091

#### **Key Points:**

- Initiation timing of Yadong-Gulu rift youngs northward (Yadong at ~13-11 Ma), but each rift system to its west initiated nearly coevally along strike
- Slab tearing released subducting slab and activated slab underthrusting that causes northward rifting acceleration
- Extraordinary earlier initiation of the Yadong rift was related to its most oblique NE-trending or outward expansion of the Himalayan arc

#### **Supporting Information:**

Supporting Information may be found in the online version of this article.

#### Correspondence to:

J. Gong, jfgong@zju.edu.cn

## Citation:

Bian, S., Gong, J., Zuza, A. V., Yang, R., Chen, L., Ji, J., et al. (2022). Along-strike variation in the initiation timing of the north-trending rifts in southern Tibe as revealed from the Yadong-Gulu rift. *Tectonics*, 41, e2021TC007091. https://doi.org/10.1029/2021TC007091

Received 28 SEP 2021 Accepted 27 MAY 2022

# Along-Strike Variation in the Initiation Timing of the North-Trending Rifts in Southern Tibet as Revealed From the Yadong-Gulu Rift

Shuang Bian<sup>1,2,3</sup>, Junfeng Gong<sup>2,3</sup> , Andrew V. Zuza<sup>4</sup> , Rong Yang<sup>2,3</sup>, Lin Chen<sup>5</sup> , Jianqing Ji<sup>6</sup>, Xiangjiang Yu<sup>7</sup> , Yihong Tian<sup>8</sup> , Zhiquan Yu<sup>2,3</sup>, Xiaogan Cheng<sup>2,3</sup>, Xiubin Lin<sup>2,3</sup> , and Hanlin Chen<sup>2,3</sup>

<sup>1</sup>State Key Laboratory of Earthquake Dynamics, Institute of Geology, China Earthquake Administration, Beijing, China, <sup>2</sup>Key Laboratory of Geoscience Big Data and Deep Resource of Zhejiang Province, School of Earth Sciences, Zhejiang University, Hangzhou, China, <sup>3</sup>Research Center for Structures in Oil and Gas Bearing Basins, Ministry of Education, Hangzhou, China, <sup>4</sup>Nevada Bureau of Mines and Geology, University of Nevada, Reno, NV, USA, <sup>5</sup>Institute of Geology and Geophysics, Chinese Academy of Sciences, Beijing, China, <sup>6</sup>School of Earth and Space Sciences, Peking University, Beijing, China, <sup>7</sup>College of Earth Sciences, Jilin University, Changchun, China, <sup>8</sup>Key Laboratory of Deep-Earth Dynamics, Ministry of Natural Resources, Institute of Geology, Chinese Academy of Geological Sciences, Beijing, China

**Abstract** A key issue in the Cenozoic evolution of the Tibetan plateau is the geodynamic drivers for north-trending rifting in southern Tibet. Recent studies have demonstrated an eastward propagation pattern for rift initiation, but the along-strike variations remain poorly resolved. Two models that predict different north-south rift kinematics include northward underthrusting or southward tearing of the Indian lithospheric slab, predicting a northward or southward propagation trend of individual rifts along strike, respectively. The Yadong-Gulu rift (YGR) is an ideal case to investigate this issue due to its long strike length (~500 km) and location above proposed slab-tear structures. Here, we compile constraints on both rift initiation and acceleration, and report new apatite fission track and (U-Th)/He thermochronological data along the southern segment of YGR. Our main findings are as follows. First, the rifts west of the YGR initiated simultaneously along strike, which we suggest is at odds with predictions of either slab-tear or slab-underthrusting models. However, most of these rifts show a northward younging pattern in rift acceleration, which may be governed by low-angle Indian slab underthrusting released by slab tearing. Second, the initiation timing of the Yadong rift is constrained at ~13-11 Ma. Combined with published constraints along strike, we demonstrate a clear northward propagation in rift initiation along the YGR. This kinematic pattern may be affected by its orientation of the most oblique northeast-trending among all rift systems or the outward expansion of the Himalayan arc.

Plain Language Summary The Himalayan-Tibetan orogen is undergoing active east-west extension under the continuous compression of the colliding Indo-Eurasia continents. This extension is manifested by a series of northward oriented (north-striking) rifts in southern Tibet, the geodynamics of which is critical in revealing the Cenozoic evolution of the Tibetan Plateau. Despite the importance, their development pattern along strike has not been well understood, leaving the mechanisms that emphasize their along-strike propagation poorly tested, such as the southward slab tearing and northward slab underthrusting models. They predict a southward or northward propagation of rifting along strike, respectively. Therefore, the along-strike propagation process of individual rifts constitutes the key factor in distinguishing the two mechanisms. In this study, we adopted thermochronological techniques to constrain the propagation of the Yadong-Gulu rift (YGR) that has the longest strike length. The results suggest that the YGR youngs northward, which is contrary to the situations of each rift system to its west that initiated nearly coevally along strike. This implies that the onset of north-trending rifts should not be significantly affected by geodynamic process in N-S direction through either slab tearing or underthrusting, while the northward younging trend of YGR is controlled largely by its oblique striking.

## 1. Introduction

The coupling between deep lithospheric processes and crustal deformation is an important issue in continental tectonics (Burchfiel et al., 1989; Fadil et al., 2006; Royden et al., 1987; Spakman & Hall, 2010). A classic

© 2022. American Geophysical Union. All Rights Reserved.

BIAN ET AL.



example of this is how deformation of the subducting Indian slab may drive development of the north-trending rifts in the Himalayan-Tibetan orogen, which are prominent structures accommodating regional east-west (E-W) extension (Figure 1; Armijo et al., 1986; Taylor & Yin, 2009; Yin, 2000, 2006). Specifically, rift development has widely been ascribed to the southward tearing (Y. Chen et al., 2015; J. T. Li & Song, 2018; Yin, 2000), northward underthrusting (Copley et al., 2011; DeCelles et al., 2002; Styron et al., 2011, 2015) or eastward lateral detachment (Bian, Gong, Zuza, et al., 2020; Webb et al., 2017) of the subducted Indian slab. Alternative models that do not invoke influence of the Indian slab include models of gravitational collapse (Molnar & Tapponnier, 1978), radial spreading (Klootwijk et al., 1985), convective thinning of lithospheric mantle models (England & Houseman, 1989), or oroclinal bending (Seeber & Armbruster, 1984) of the Himalayan arc and oblique convergence of the Indian continent models (McCaffrey & Nabelek, 1998). However, recent studies revealed a monotonic eastward younging trend of the rift systems, which was interpreted as evidence for an eastward propagation of the lateral detachment of the Indian slab (Bian, Gong, Zuza, et al., 2020).

The E-W spatiotemporal pattern of rift initiation does not uniquely constrain the applicability of the slab longitudinal tearing or underthrusting mechanisms, which are predicted to impact the along strike (i.e., generally north-south) propagation history of individual rift systems. Slab tearing predicts a north-to-south propagation of rifting as tearing initiates at the northern tip of subducting Indian slab and migrates southward. This model is mainly based on the significant lateral variations observed across the underthrusting Indian lithospheric slab by geophysical observation (Y. Chen et al., 2015; Duan et al., 2017; J. T. Li & Song, 2018; Z. Liu et al., 2020; Pei et al., 2016; Si et al., 2019; G. Wang et al., 2017; C. L. Wu et al., 2019; Xiao et al., 2007) and the spatiotemporal consistency among rift systems and Miocene ultrapotassic rocks (X. Y. Guo et al., 2018; Z. F. Guo & Wilson, 2019; Hou et al., 2006; R. Wang et al., 2015, 2021; Yan et al., 2019). In contrast, slab underthrusting predicts a south-to-north propagation of rift initiation or acceleration in response to the northward insertion of a tapering Indian slab beneath southern Tibet (DeCelles et al., 2002; Lee et al., 2011; Styron et al., 2015). This model fits with the observation that rifting is more prominent to the south of the Bangong-Nujiang suture zone due to a thicker and wider Indian slab compared to that on the north (Figure 1a; DeCelles et al., 2002; Yin, 2000).

The key to the validity of any E-W extension model is that it must reasonably explain the spatiotemporal pattern of rifting (e.g., Bian, Gong, Zuza, et al., 2020 and references therein). In this regard, the development process of individual rift systems is crucial evidence to evaluate the slab southward tearing vs. northward underthrusting models. However, the along-strike variation in the timing of rift initiation remains obscure, although Styron et al. (2015) documented a northward younging trend for rift acceleration along the Lunggar rift (Figure 1a). The Yadong-Gulu rift (YGR), located in the central-east part of the orogen, is the longest of the rift systems (~500 km) spanning the Himalayas and Lhasa terrace in surface, and is thus ideal to test along-strike patterns of the extensional history (Figure 1a). Furthermore, it is the only rift that is spatially located above the hypothesized slab tearing phenomenon (J. T. Li & Song, 2018; T1 in Figure 1a). On the northern segment of the YGR (Gulu rift, p in Figure 1a), apatite (U-Th)/He (AHe) data indicated onset of rifting at  $\sim$ 7–5 Ma (Stockli et al., 2002). On the central segment, mica and K-feldspar 40Ar/39Ar data from the footwall of Nyainqentanghla ductile shear zone (o in Figure 1a) recorded a rapid cooling event at ~8 Ma, indicating the onset of extension (Harrison et al., 1995). An 8.7 Ma NE-striking leucogranitic dike intruding the basement of the Nyainqentanghla range offers further constraints for the age of normal fault initiation (J. L. D. Kapp et al., 2005). Further south, in the Ringbung rift (n in Figure 1a), the onset of normal faulting was constrained before 7 Ma recorded by the emplacement and subsequent rapid cooling of the leucogranite (Ratschbacher et al., 2011). The Gyanze rift (m in Figure 1a) initiated before ~10.8 Ma based on the age of a north-striking granite-porphyry dyke (Ratschbacher et al., 2011). In general, for the north and central segments of the YGR, it seems that rift initiation timing becomes older. However, on the southern segment (Yadong rift, 1 in Figure 1a), there still lacks any direct constraints on the activities of rifting, despite important indirect evidence yielding an upper limit by cutting the South Tibet Detachment (STD) during two decades of insightful exploration (e.g., ~10 or ~13-11 Ma; S. Y. Chen et al., 2022; Edwards & Harrison, 1997; Xu et al., 2013).

In this study, we report new apatite fission track (AFT) and (U-Th)/He thermochronological data collected along four elevation profiles across the southern Yadong rift (Figure 2). Age-elevation profiles and thermokinematic modeling of these data are used to reconstruct the activation history of the Yadong rift, based on which we explore the along-strike variation in the rift initiation timing. Furthermore, by compiling available published data we construct a general trend in along-strike variation for all rift systems in southern Tibet. This sheds new light

BIAN ET AL. 2 of 23



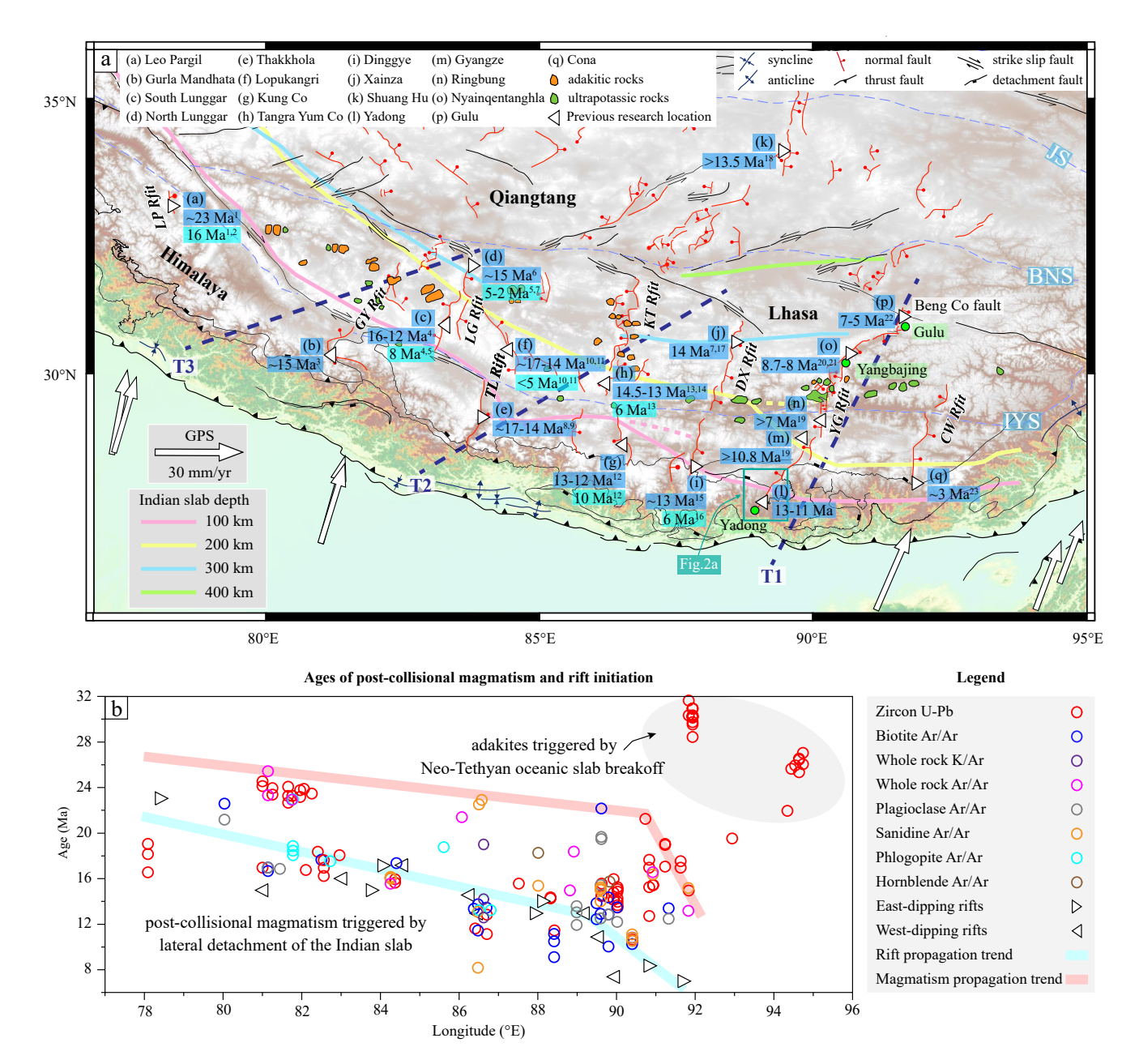


Figure 1. (a) Tectonic map of the Himalayan-Tibetan system (modified from Taylor & Yin, 2009; Webb et al., 2017). Triangles denote the locations of previous studies of north-trending rifts. The numbers in the blue boxes represent the initiation timing and in the pale blue-green boxes represent the later stage of rift acceleration timing. The corresponding references are marked as numbers in superscript form, including (1) Langille et al. (2012); (2) Thiede et al. (2006); (3) Murphy and Copeland (2005); (4) Styron et al. (2013); (5) Styron et al. (2015); (6) P. Kapp et al. (2008); (7) Sundell et al. (2013); (8) Larson et al. (2020); (9) Coleman and Hodges (1995); (10) Sanchez et al. (2010); (11) Laskowski et al. (2017); (12) Lee et al. (2011); (13) Dewane et al. (2006); (14) Wolff et al. (2019); (15) J. J. Zhang and Guo (2007); (16) Kali et al. (2010); (17) Hager et al. (2009); (18) Blisniuk et al. (2001); (19) Ratschbacher et al. (2011); (20) Harrison et al. (1995); (21) J. L. D. Kapp et al. (2005); (22) Stockli et al. (2002); (23) Bian, Gong, Zuza, et al. (2020). The dashed blue thick lines (T1, T2, and T3) indicate sites of the three possible slab tearing following J. T. Li and Song (2018). T1 strikes NNE and is spatially matched well with the Yadong-Gulu rift (YGR), while T2 and T3 strike NE, crossing local rifts with poor spatial match. The pink, yellow, light blue and green thick lines indicate the current depth contours of the Indian slab at 100, 200, 300, and 400 km, respectively (C. Li et al., 2008). Dashed pink and yellow thick lines illustrate deduced offsets. The white arrows are GPS velocity fields with respect to Eurasian plate after S. G. Wang and Shen (2020). Key to symbols: IYS, Indus-Yarlung suture; BNS, Bangong-Nujiang suture; JS, Jinsha suture; AMS, Anyimaqen-Kunlun-Muztagh suture; CW Rift, Cona-Woka Rift; YG Rift, Yadong-Gulu Rift; DX Rift, Dinggye-Xainza Rift; KT Rift, Kung Co-Tangra Yun Co Rift; TL Rift, Thakkhola-Lopukangri Rift; LG Rift, Lunggar Rift; GY Rift, Gurla Mandhata-Yare Rift; LP Rift, Leo Pargil Rift. (b) Longitudinal variations in post-collisional adaktitic and ultrapotassic rocks and rift initiation timing (Bian, Gong, Zuza, et al., 2020; Z. F. Guo et al., 2015; L. Y. Zhang et al., 2014, and references therein). Adaktitic rocks can be divide into two groups, characterized by different fractionation evolutions of light and medium rare earth elements (Lu et al., 2020). The eastern cluster of adaktitic rocks was triggered by the breakoff of Neo-Tethyan oceanic slab, whereas others by lateral detachment of the Indian continental slab (Lin et al., 2021; Lu et al., 2020). The eastward-younging trend of post-collisional magmatism slowed down crossing the Yadong rift, which is consistent with the deceleration of the eastward propagation of rifting.

BIAN ET AL. 3 of 23

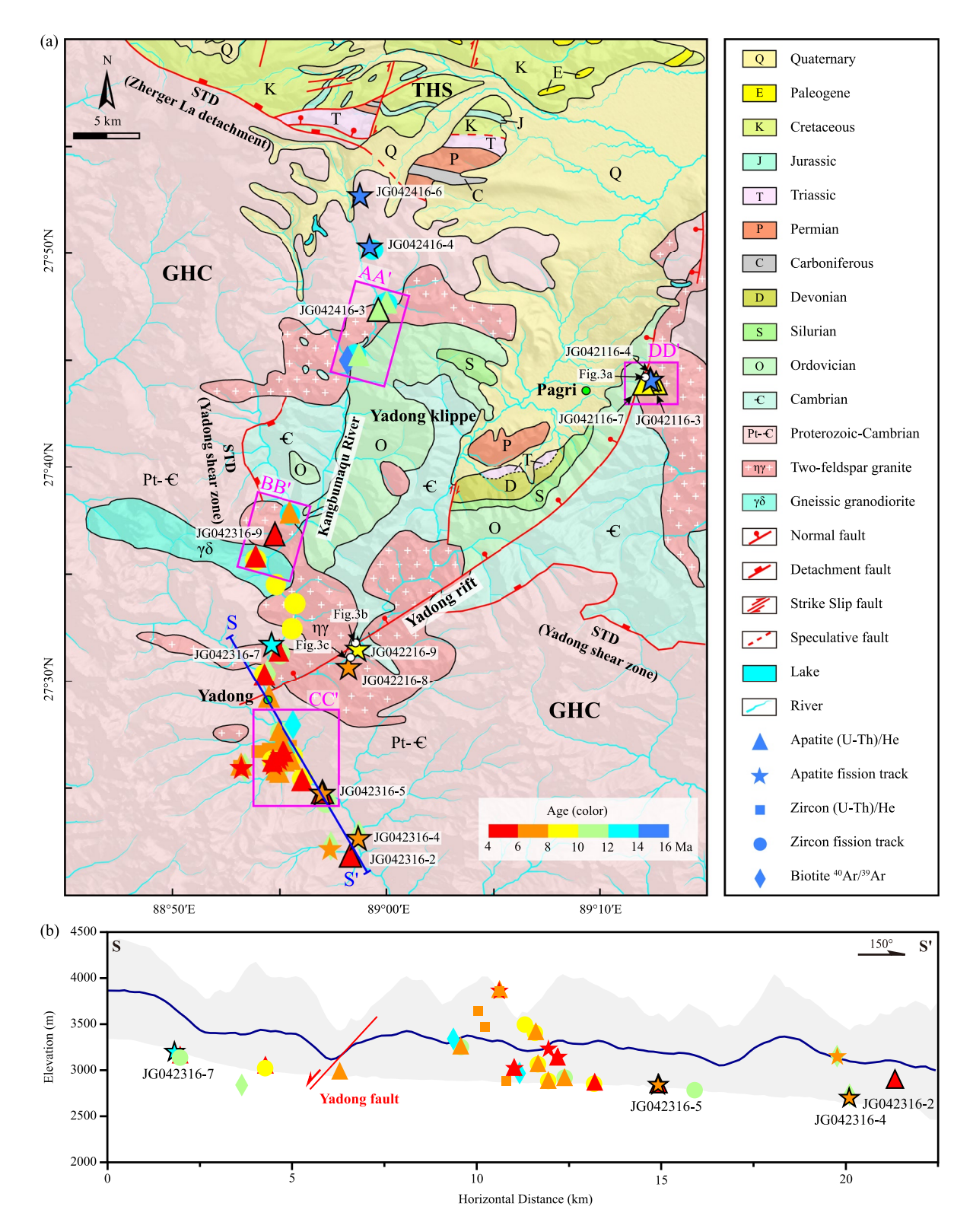
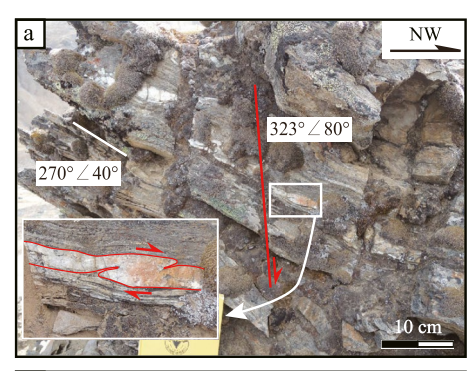


Figure 2. (a) Regional geological map of the Yadong area with compiled low-temperature thermochronological ages. The map was modified from China University of Geosciences Beijing (2002). The profiles AA' and BB' in the hanging wall records older ages than those of the CC' and DD' profiles crossing the rift. (b) Swath profile of topography across the Yadong rift (S-S'on Figure 2a) with sample locations that from Dong et al. (2020), Gong et al. (2012), A. Wang et al. (2019), and Xu et al. (2013) and this study. Our new data are marked by black lines. The color of samples denotes age values. Across the Yadong fault, the hanging wall is closer to the outer STD, and is thus higher than the footwall since movement along the outer STD has caused southward wedging of GHC prior to rifting. Key to symbols: STD, South Tibet Detachment; GHC, Greater Himalayan Crystalline Complex; THS, Tethyan Himalayan Sequence.

BIAN ET AL. 4 of 23







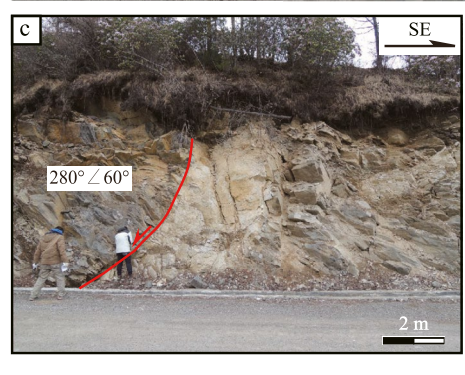


**Figure 3.** Field observations of the Yadong fault. (a) Outcrop photograph indicating top-to-the-west ductile shearing of a quartz vein and subsequent high-angle normal faulting. (b) Photograph of east-dipping faults cross-cutting the leucogranitic dike. We interpret that the fault planes were rotated westward (counter-clockwise in this photo) due to progressive footwall rotation, and thus the fault originally dipped west. (c) Outcrop photographs of listric faults cutting leucogranite. Attitudes are expressed as dip direction and dip angle. The photograph locations are shown in Figure 2a.

on the debates over the mechanisms of rift formation in Tibet to evaluate the applicability for slab tearing and underthrusting models.

## 2. Geologic Setting

A series of north-trending rifts developed across both the Himalayan orogen and Tibetan plateau (Figure 1a), which vary systematically in spacing and strike. The rift spacing decreases from south to north (Armijo et al., 1986; Yin, 2000) and the strike varies from northwest in the west to northeast in the east (P. Kapp & Guynn, 2004; Yin, 2006), implying a unified dynamic mechanism of rifting. South of the Bangong-Nujiang suture zone, E-W extension is mainly accommodated by eight rift systems (Figure 1a), which are approximately continuously distributed along their strikes, with long surface expressions. Among them, the northeast-trending YGR is one of the most prominent rifts, which is roughly distributed along the 90°E longitude, extending a total length of ~500 km (Figure 1a). The whole rift zone starts in the Nepal Himalaya in the south and extends northward along the Nyainqentanghla to the Lhasa terrane, which crosses the STD, the Indus-Yarlung suture zone (IYS) and terminates at the Beng Co left-slip fault (Armijo et al., 1986; Chevalier et al., 2020; Ha et al., 2019; C. D. Wu et al., 1998; Z. H. Wu et al., 2015).

The YGR can be divided into three segments according to the spatial variation of the main boundary faults (Figure 1a; Armijo et al., 1986; Chevalier et al., 2020; Z. H. Wu et al., 2015). In the northern segment, north of the Yangbajing, there is a continuous east-dipping main boundary fault system with an abrupt bend from north-striking to northeast-striking, marking a sudden transition from the predominant normal faulting to the combination of normal and strike-slip faulting. In the central segment, between the Yangbajing and IYS, faults are relatively scattered and dip in opposite directions. In the southern segment, south of the IYS, the rift consists of three grabens in en-echelon arrangement, which are bounded by several west-dipping normal faults. Along the strike of YGR, Late Quaternary E-W extension rates have obvious spatial variations, which are characterized by faster rates in the northern segment (3-6 mm/yr) than the central and southern segments (0.6-1.7 mm/yr) (Chevalier et al., 2020; Ha et al., 2019; S. G. Wang et al., 2020; Z. H. Wu et al., 2015, 2004; G. Yang et al., 2020; Zuo et al., 2021).

This study focuses on the southernmost segment of the Yadong rift (Figures 1a and 2), which consists of a west-dipping normal fault that bounds the east side of the Pagri graben. Field observations of the Yadong rift indicate a dominant top-to-the-west deformation (Figure 3). The Yadong rift was considered to cut the inner STD at Zherger La (termed as Zherger La detach-

ment, Figure 2) based on the apparent, left-lateral separation (Figure 1a, Burchfiel et al., 1992). Alternatively, C. D. Wu et al. (1998) suggested that the offset is expression of a north-northeast striking west-facing lateral ramp. Farther south, the Yadong rift crosses the Yadong klippe that is bounded by ductile deformation of the outer STD (termed as Yadong shear zone, Dong et al., 2020; Z. C. Liu et al., 2017; Xu et al., 2013). Lithologies in the Yadong area are comprised of the Greater Himalayan Crystalline Complex (GHC) and Tethyan Himalayan Sequence (THS) that are structurally separated by the STD (Figure 2; Xu et al., 2013; A. Wang et al., 2019). The GHC consists of Precambrian metamorphic rocks including migmatites, marbles, leptynite, gneisses and schists (Figure 2), which have undergone strong migmatization and were intruded by numerous granites. Above the GHC, the THS consists of Cambrian-Triassic sedimentary rocks including schists, sandstones, limestones, calcisiltites, shales, and phyllites.

BIAN ET AL. 5 of 23



In the Yadong region, previous studies have reported thermochronological data (Dong et al., 2020; Gong et al., 2012; Z. C. Liu et al., 2017; A. Wang et al., 2019; Xu et al., 2013), including zircon and monazite U-Pb, biotite <sup>40</sup>Ar/<sup>39</sup>Ar (BtAr), zircon fission track (ZFT), (U-Th)/He (ZHe), AFT and AHe (Table S1 in Supporting Information S1). Most sampling was focused along the Kangbumaqu River valley draining through the GHC (Figure 2). Among them, zircon and monazite U-Pb data from undeformed leucogranites exposed in the Yadong klippe suggested that ductile motion along the Yadong shear zone had ceased by ~20 Ma (Dong et al., 2020; Z. C. Liu et al., 2017), whereas zircon U-Pb data of deformed gneiss sample collected from the footwall of the Zherger La detachment suggested that motion along the Zherger La detachment continued after ~16.6 Ma (Dong et al., 2020). Movement along the STD has caused southward wedging of the GHC (e.g., Xu et al., 2013; Yin, 2006). In addition, low-temperature thermochronological data record rapid exhumation of the GHC as documented by BtAr ages at ~13–11 Ma, ZFT ages at ~10–8 Ma, and AFT and AHe at ~8–5 Ma. It remains ambiguous whether the rapid exhumation is driven by the activities of the STD (Dong et al., 2020; A. Wang et al., 2019; Xu et al., 2013) or the Yadong rift (Dong et al., 2020).

# 3. Low-Temperature Thermochronometry

#### 3.1. Sampling

To constrain the activation history of the Yadong rift, 13 new samples were collected for low-temperature thermochronology along four profiles (Figure 2) with detailed descriptions in Table 1. The north-trending AA' and BB' profiles are in the hanging wall of the Yadong rift, along which two AHe (JG042416-3 and JG042316-9) and two AFT (JG042416-4 and JG042416-6) samples were collected. The north-trending CC' profile starts at the footwall and then crosses the Yadong rift. Two AHe (JG042316-2 and JG042316-5) and five AFT (JG042216-8, JG042216-9, JG042316-4, JG042316-5, and JG042316-7) samples were collected along this profile. The west-trending DD' profile locates to the east of the Pagri town, with an average elevation of ~4,800 m. Three AHe (JG042116-3, JG042116-4, and JG042116-7) and one AFT (JG042116-4) samples were collected in the footwall from a steep ridge.

#### 3.2. Methods

## 3.2.1. Apatite (U-Th)/He Thermochronology

Apatite grains were separated by conventional magnetic and heavy liquid, and then euhedral and inclusion-free grains were handpicked. At least three grains larger than 60 µm in both length and width were selected for each

<b>Table 1</b> Sample Description and Summary of Thermochronological Results							
Sample	Lithology	Latitude (°N)	Longitude (°E)	Elevation (m)	Profile	AHe age (Ma)	AFT age (Ma)
JG042416-3	Granite	27.7854	88.9936	4,173	AA'	$11.18 \pm 0.96$	
JG042416-4	Migmatite	27.8376	88.9860	4,501	AA'		$14.18 \pm 1.48$
JG042416-6	Basic granulite	27.8791	88.9778	4,744	AA'		$15.37 \pm 1.43$
JG042316-9	Granite	27.6038	88.9166	3,552	BB'	$5.65 \pm 1.17$	
JG042216-8	Granite	27.5104	88.9672	3,570	CC'		$8.00 \pm 0.78$
JG042216-9	Granite	27.5243	88.9767	3,413	CC'		$9.41 \pm 1.09$
JG042316-2	Schist	27.3627	88.9715	2,819	CC'	$5.84 \pm 0.89$	
JG042316-4	Granitic gneiss	27.3771	88.9762	2,691	CC'		$7.73 \pm 0.83$
JG042316-5	Granitic gneiss	27.4121	88.9485	2,847	CC'	$5.05 \pm 0.13$	$6.27 \pm 0.79$
JG042316-7	Granite	27.5257	88.9118	3,141	CC'		$13.22 \pm 1.48$
JG042116-3	Granite	27.7285	89.2089	4,749	DD'	$9.15 \pm 0.04$	
JG042116-4	Granite	27.7306	89.2059	4,830	DD'	$9.92 \pm 1.75$	$14.94 \pm 1.71$
JG042116-7	Granite	27.7302	89.2013	4,680	DD'	$9.57 \pm 0.93$	

BIAN ET AL. 6 of 23



sample except samples JG042116-3 and JG042316-5 with one and two grains, respectively. Selected apatite separates were degassed by a diode laser heating (in the range of  $800^{\circ}\text{C}-900^{\circ}\text{C}$ ) and the released gas was measured on a magnet sector field mass spectrometer equipped with a Baur-Signer ion source at ETH Zurich to determine the <sup>4</sup>He abundances. The U, Th, and Sm concentrations were then measured on an inductively coupled plasma quadrupole mass spectrometer (PerkinElmer ElanDRC-e). The age calculation was processed and corrected for  $\alpha$ -ejection, Ft, following Ketcham et al. (2011).

## 3.2.2. Apatite Fission Track Thermochronology

Apatite samples were analyzed following the external detector method (Hurford & Green, 1983). Separated apatite grains were mounted in epoxy, polished and then etched for 20 s in a 5.5 M HNO<sub>3</sub> solution at 21°C. Etched samples were covered with U-poor muscovite sheets and irradiated together with CN5 glass standards at the Oregon State University reactor. After irradiation, the muscovite sheets and glass dosimeter were etched in 40% HF for 40 min at the room temperature. Specimens were then counted by a Zeiss microscope at a magnification of 1,000X. In general, at least 20 grains were analyzed for each sample. AFT ages were calculated using a zeta factor ( $\zeta$ ) of 343.62  $\pm$  14.25 determined by multiple analyses of the Durango apatite standards.

#### 3.3. Results

Seven AHe samples with mean ages ranging from  $5.05 \pm 0.13$  to  $11.18 \pm 0.96$  Ma (Table 1 and Table S2 in Supporting Information S1) are distributed on four profiles (Figure 2a). Among these, samples JG042416-3 and JG042316-9 in the hanging wall of the Yadong rift from profiles AA' and BB' yielded ages of  $11.18 \pm 0.96$  and  $5.65 \pm 1.17$  Ma, respectively. The ages of samples JG042316-2 and JG042316-5 from profile CC' are  $5.84 \pm 0.89$  and  $5.05 \pm 0.13$  Ma. Three AHe ages from profile DD' vary in a small range between  $9.15 \pm 0.04$  and  $9.92 \pm 1.75$  Ma.

All eight AFT samples (Figure 2a) passed the  $\chi^2$  test (P( $\chi^2$ ) > 5%, Galbraith & Green, 1990) and yielded ages between 6.27  $\pm$  0.79 to 15.37  $\pm$  1.43 Ma (Table 1 and Table S3 in Supporting Information S1). Three AFT ages in the hanging wall vary from 13.22  $\pm$  1.48 to 15.37  $\pm$  1.43 Ma, which is older than those in the footwall. Four AFT ages around the profile CC' are similar, ranging from 6.27  $\pm$  0.79 to 9.41  $\pm$  1.09 Ma. In addition, sample JG042116-4 from profile DD' yielded an age of 14.94  $\pm$  1.71 Ma.

## 4. Interpretation

## 4.1. Age-Elevation Relationship (AER)

We use new thermochronological ages, combined with published data (Figure 2), to constrain the activation history of the Yadong rift based on the observed AER. The horizontal distances of samples within the four profiles are all within 7 km, which meets the standard of limited horizontal distance of the samples analyzed in a vertical profile (<10 km, Braun, 2002). Both profiles AA' and BB' are located at the hanging wall of the Yadong rift, and thus the simplest interpretation is that their exhumation was not directly impacted by rifting. The profile AA', near the Zherger La detachment (local segment of inner STD), shows high exhumation rate (~0.4 mm/a) between ~14 and ~11 Ma (Figure 4a). This could be attributed to the activities of the Zherger La detachment, whose movement was previously interpreted to be continuously active until ~11 Ma (Dong et al., 2020; Gong et al., 2012; A. Wang et al., 2019). On the BB' profile, near the Yadong shear zone (outer STD), AHe and ZFT ages reveal a consistent exhumation rate of ~0.1 mm/yr between ~13 and ~4 Ma (Figure 4b). This slow regional exhumation rate is comparable with the reported data from adjacent areas, such as the central-east Himalaya near the Gyirong (Shen et al., 2016), Ama Drime (Kali et al., 2010), Nimu (Dai et al., 2021), Cona (Bian, Gong, Zuza, et al., 2020), and southern Tibet near the Lhasa (Tremblay et al., 2015), which implies that it has not experienced structural exhumation caused by the Yadong shear zone. This observation is consistent with the proposal that the Yadong shear zone had ceased before ~20 Ma (Dong et al., 2020; Z. C. Liu et al., 2017).

Compared with profile BB', the profile CC' is located further away from the outer and inner STD (Yadong shear zone and Zherger La detachment), and is thus possibly less affected by their activities. The profile CC' is located within the footwall of the secondary fault of Yadong rift, where leucogranitic dikes were cut by west-dipping faults (Figures 3b and 3c). The fault strike is also consistent with that of the main fault of Yadong

BIAN ET AL. 7 of 23



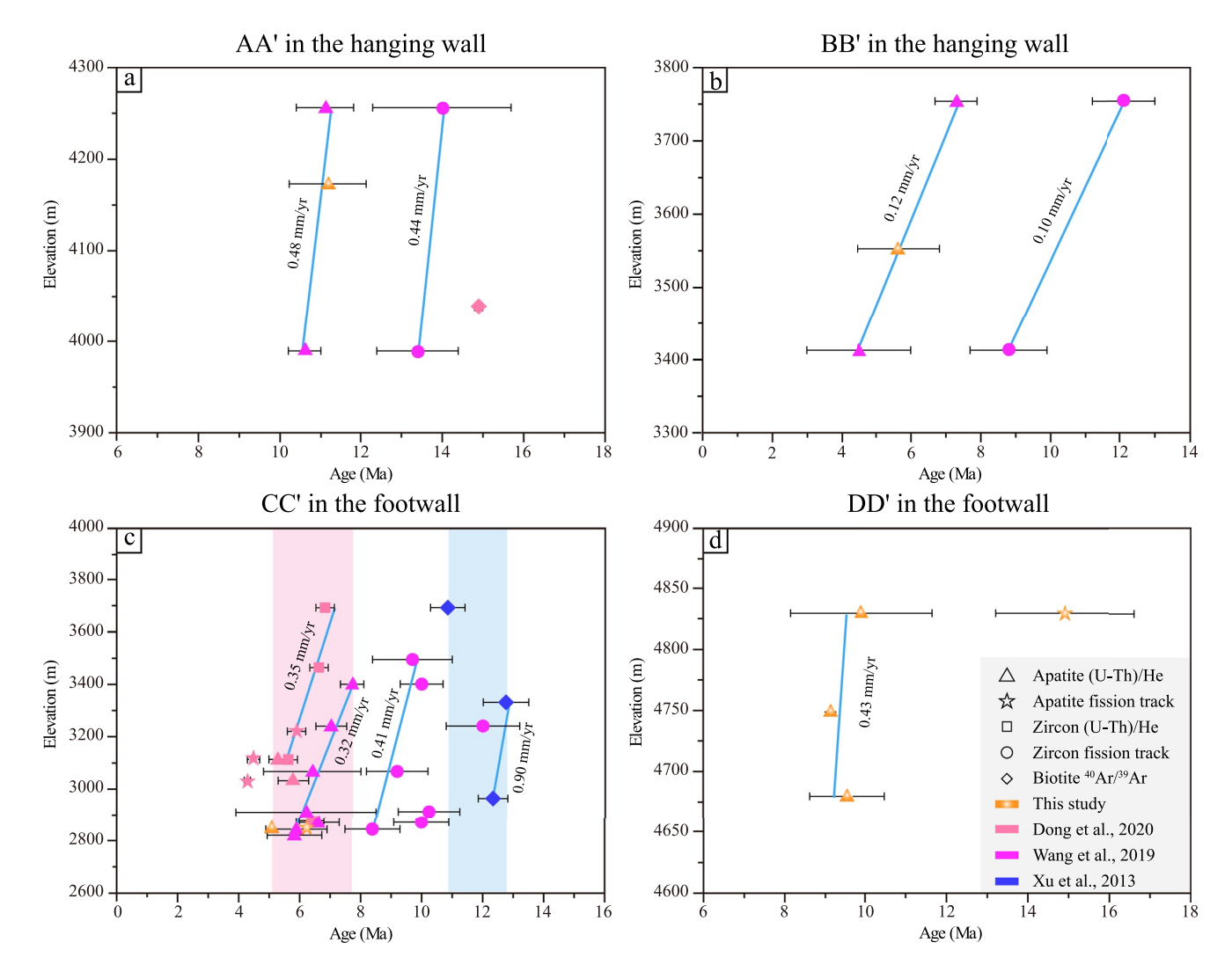


Figure 4. Age-elevation plots of the profile AA' (a), BB' (b), CC' (c) and DD' (d). The profile AA' shows high exhumation rate ( $\sim$ 0.4 mm/a), which could be attributed to the activities of the Zherger La detachment (inner STD). The exhumation rate from the profile BB' in the hanging wall is  $\sim$ 0.1 mm/yr, while the exhumation rate from the profile CC' and DD' in the footwall is  $\sim$ 0.9-0.3 mm/yr. The difference in the exhumation rate crossing the rift constrains the rapid exhumation of rifting at  $\sim$ 13-11 Ma. Shading shows that BtAr and AHe data concentrated at  $\sim$ 13-11 and  $\sim$ 8-5 Ma, respectively.

rift. Therefore, it was treated as a southward extension of the main fault. The exhumation on the profile CC' likely reflects the activity of the Yadong rift. On this profile, BtAr data record a rapid exhumation rate of ~0.9 mm/yr between ~13 and 11 Ma. In addition, the AERs of AHe, ZHe, and ZFT are very similar, showing an apparent exhumation rate of ~0.4–0.3 mm/yr from ~10 to 5 Ma (Figure 4c). Taking into account the influence of sample elevations, BtAr and AHe data (Dong et al., 2020; Gong et al., 2012; A. Wang et al., 2019; Xu et al., 2013) have an age difference of ~5–8 Myr, which implies a high cooling rate of ~34–55°C/Myr (adopting closure temperatures of 350°C for BtAr and 75°C for AHe, McDougall & Harrison, 1999; Wolf et al., 1996). Assuming a geothermal gradient of ~23–40°C/km (Francheteau et al., 1984), the cooling rate corresponds to an exhumation rate of ~0.9–2.4 mm/yr.

To the north of the profile CC' (in the north of SS'), two samples in the hanging wall yielded AHe ages of 4.2 and 5.5 Ma, and ZFT ages of 9.4 and 11.5 Ma (Figure 2), which implies a slow exhumation rate of  $\sim$ 0.1 mm/ yr at  $\sim$ 12–4 Ma based on the AER, matching that of the profile BB'. They both reveal early stage slow exhumation rate in the hanging wall during the initial activation of the Yadong rift. This interpretation is further supported by an older AFT age (13.22  $\pm$  1.48 Ma) in the hanging wall than those in the footwall (7.73  $\pm$  0.83 and 6.27  $\pm$  0.79 Ma).

BIAN ET AL. 8 of 23



On the profile DD' (leading edge of the footwall of Yadong rift), samples from different elevations exhibit very similar AHe ages, which reflects rapid exhumation at a rate of  $\sim$ 0.4 mm/yr at  $\sim$ 9 Ma (Figure 4d). This trend is consistent with the AERs on the profile CC'. Therefore, we interpret that these differences of the exhumation rates across the Yadong rift reflect top-to-the-west sense motion of the Yadong rifting (Figure 3) and rapid footwall exhumation.

## 4.2. Thermokinematic Modeling

#### 4.2.1. Modeling Approach

To better constrain the activation history of the rift, we conducted PECUBE thermokinematic modeling (Braun, 2003) of the data from profiles CC' and DD', respectively. PECUBE is a finite-element code solving the three-dimensional heat transport equation to predict thermal structure, landscape evolution, and tectonics history (Braun, 2003; Glotzbach et al., 2008; Herman et al., 2010; King et al., 2016). The code can be used for inverse modeling coupled to a two-stage inversion method (i.e., Neighborhood Algorithm, Sambridge, 1999a, 1999b), which divides the parameter space as a set of Voronoi cells (Voronoi, 1909) and searches the optimized cell by iterations process. The first step is to generate sampling points to define the new Voronoi cells using iterative search method in a random fashion. The purpose is to find a series of parameters values that minimize the misfit between modeled data and observations. In our approach, the weighted least squares misfit function  $\psi$  is expressed as (Braun et al., 2006, 2012):

$$\Psi = \frac{1}{N} \sqrt{\sum_{i}^{N} \frac{\left(i\alpha_{\text{mod}} - i\alpha_{dat}\right)^{2}}{i\alpha^{2}}}$$

where N is the number of measured ages;  ${}^{i}\alpha$  is the uncertainty on the data;  ${}^{i}\alpha_{mod}$  and  ${}^{i}\alpha_{dat}$  are the predicted and observed values, respectively. The second stage is to appraise model ensemble generated by resampling in the form of marginal probability density functions. Recently, neighborhood algorithm is widely used in numerical thermal-kinematic modeling because of its efficient computational efficiency (e.g., Campani et al., 2010; Glotzbach et al., 2011; Valla et al., 2010; Wolff et al., 2020, 2019).

In inverse numerical modeling, estimating the best-fit model to the observed data requires defining the dimensionality of the model, such as the number of exhumation and relief scenarios. However, one of the major unknown concerns what dimensionality is appropriate (Akaike, 1974; Glotzbach et al., 2011; Schwarz, 1978). It is an important issue of balancing improved model fits of the thermochronology data and increasing the complexity of the model with additional parameters. The Bayesian information criterion (BIC, Schwarz, 1978) provides a straightforward way to assess the appropriate model complexity, which is defined as:

$$BIC = -2 \operatorname{Ln}(L) + k \ln(n)$$

where Ln(L) is the log-likelihood for the model, and k and n are the number of free parameters and observations, respectively.

Here, we tested a set of inversions with different degrees of model complexity. The BIC values were first calculated following the method described in Glotzbach et al. (2011), to select appropriate model dimensionality. The preferred model matching the observed thermochronological data was defined by the lowest BIC value. Then, the validity of this model is evaluated by scatter plots and marginal probability density functions. The best-fit model with the lowest misfit value represents the optimal parameter combinations.

## 4.2.2. Model Setup

For profiles CC' and DD', we performed six inverse models with various paleo-topography and fault kinematics, respectively. All scenarios were run over 20 Myr with 30,100 models distributed in 300 iterations. A high resampling ratio of 90% was set, ensuring sufficient search of the parameter space. The paleo-topography was modeled by the vertical offset (Zt) and relief factor (Rt), such that:

$$h(x, y, t) = Zt + Rt \times h(x, y)$$

BIAN ET AL. 9 of 23

where h(x, y, t) is the paleo-topography at time t and h(x, y) is the present-day topography. The vertical offset is incorporated to the topography to keep a given elevation. Recent studies in the Mount Everest region west of the Yadong suggested a proto-plateau with a mean elevation of ~5 km from 20 Ma (Carrapa et al., 2016). The relief factor, defined as the relief changes between past and present-day topographies (Glotzbach et al., 2011; Valla et al., 2010; van der Beek et al., 2010), was adopted to represent the effect of surface relief. In the modeling, the Yadong normal fault is simplified as a straight plane striking 230° and dipping 50°NW, with the footwall moving southeastward during northwest hanging wall displacement.

Relief scenarios include steady-state or varying proto-plateau topography, with the relief factor ranging between 1 and 0. Faulting scenarios include one- and two-phase exhumation scenarios with associated slip rates ( $E_1$  and  $E_2$ , range: 5–0 mm/yr), onset time ( $T_1$ ) and transition time ( $T_2$ ). The one-phase scenario assumes a constant slip rate ( $E_1$ ) between  $T_1$  and 0 Ma, while the two-phase scenario incorporated a second exhumation phase ( $E_2$ ) by assuming a  $T_2$  between  $T_1$  and 0 Ma. All inverted parameters are listed in Tables S4 and S5 in Supporting Information S1, together with the best-fit models, and resulting BIC values. A full summary of the input thermokine-matic and elastic parameters are listed in Table S6 in Supporting Information S1, guided by values used in similar studies (Styron et al., 2013; Tremblay et al., 2015).

## 4.2.3. Inversion Results

On the profile DD', the onset time of normal faulting had been constrained to prior to  $\sim$ 9 Ma from the AER (Figure 4d). Accordingly, we adopted a range of 20–8 Ma for the  $T_1$  and a range of 8–0 Ma for the  $T_2$ . Two steady-state topography inversions were performed with one (Run D1) or two (Run D2) exhumation phases, which yielded BIC values of 5.85 or 10.27, respectively. The proto-plateau inversions include an initial topography with a mean elevation of 5 km (Carrapa et al., 2016) imposed 10% (Rt = 0.1) of present-day relief (Run D3, D4) or varying relief factor (Run D5, D6). Since modeling started, the elevation was progressively lowered by faulting. Inversion results (Table S4 in Supporting Information S1) suggested that the BIC values were maximized from 6.99 to 10.90 by adding free parameters (i.e., relief factor and exhumation phase).

Judged by the lowest BIC value, the most favorable model lies in the one-phase exhumation faulting process that evolved from a steady-state topography background (Run D1). In this scenario, results of the best-fit model (misfit = 0.09) suggest a pulse of rapid exhumation beginning at  $\sim 11.01$  Ma with a slip rate of  $\sim 1.14$  mm/yr,

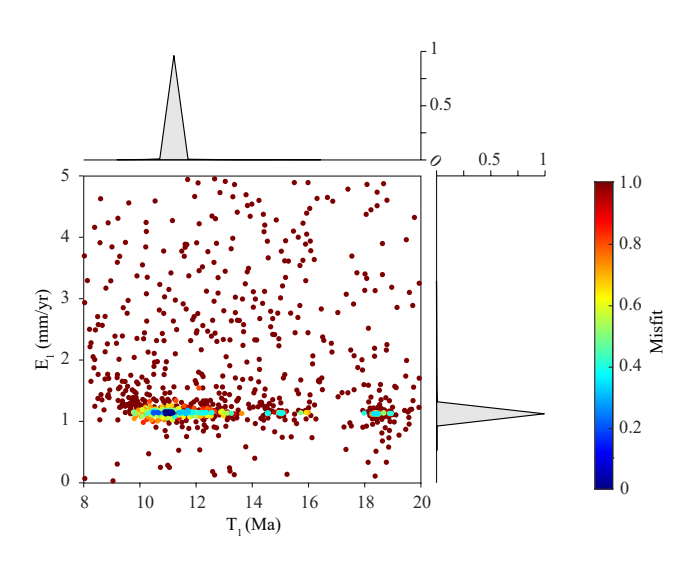


**Figure 5.** Scatter plots for onset time of faulting  $(T_1)$  and slip rate  $(E_1)$  from inversion Run D1 on the profile DD'. Each dot corresponds to an individual model. Colors reflect the misfit value between predicted and observed data. The models with minor misfit converge to a very small range, implying a convergent result. Probability density functions are shown for each parameter, which are in unimodal pattern that indicates the effective control on the faulting history.

which is a reliable estimate for the development history of the Yadong rift based on the following aspects. First, results of each scatter plot converge to the concentrated value of the best-fit model (Figure 5). Second, the predicted ages from the best fitting model are consistent with the observed data (Figure S1 in Supporting Information S1) within the error range. Third, each probability density function is in unimodal pattern with peaks at the concentrated value of the scatter plots (Figure 5), indicating the effective control on the faulting history.

On the profile CC', low-temperature thermochronological data present an inverse pattern at a certain extent (Figure 4c). Specifically, some of ZHe ages (Dong et al., 2020) are younger than AHe ages (Dong et al., 2020; A. Wang et al., 2019). This inversion in apparent closure temperatures for ZHe and AHe might be affected by alpha damage (Guenthner et al., 2013, 2014). Suites of zircon He dates contain some single grains that span a large range in eU (Figure S2 in Supporting Information S1). Three grains contain high eU concentration above 1,500 ppm, and others show clear negative date vs. eU correlation, which suggests that these grains might be damaged (Guenthner et al., 2013) and could possess closure temperatures as low as  $\sim$ 50°C (e.g., Johnson et al., 2017). Considering that the PECUBE inversions do not take into account the effects of radiation damage, we run different inversions on this profile excluding those data. The model configurations are the same as those on the profile DD'.  $T_1$  was set between 10 and 20 Ma based on the preliminary analysis of published BtAr data, and  $T_2$  was set between 15 and 0 Ma.

BIAN ET AL. 10 of 23



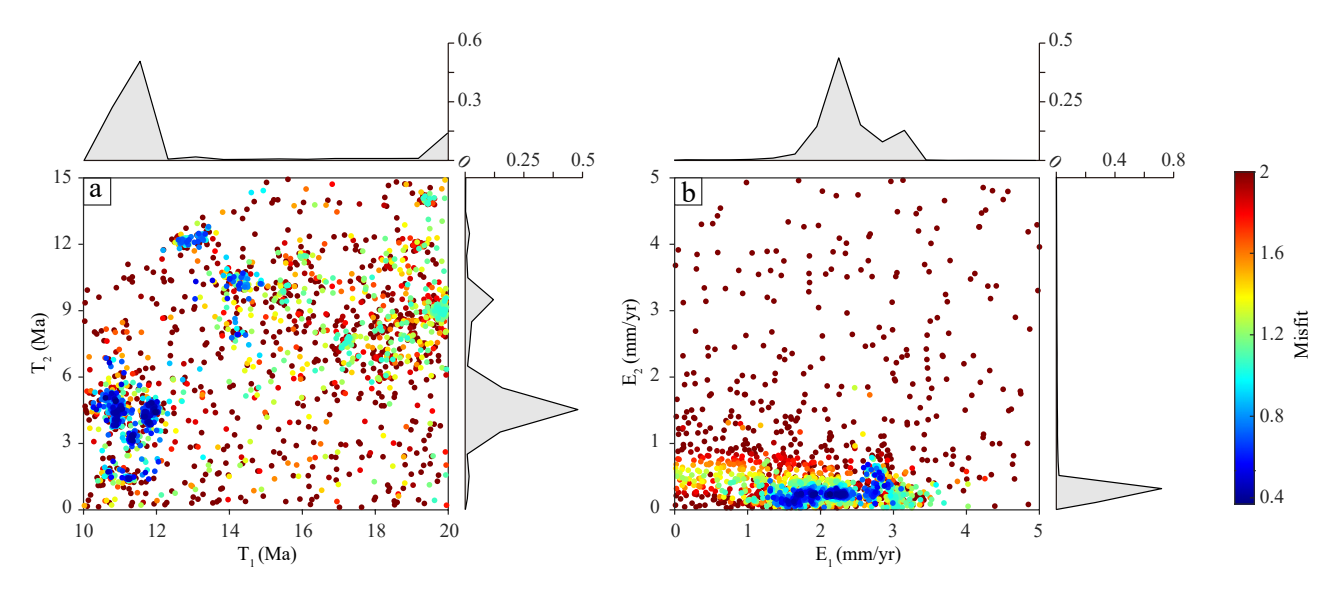


**Figure 6.** Scatter plots for inversion model from inversion Run C4 on the profile CC'. (a) Onset timing  $(T_1)$  and transection time  $(T_2)$ . (b) Slip rates of faulting in the first  $(E_1)$  and the second  $(E_2)$  phase. Both the scatter plots and unimodal marginal probability density functions indicate the effective control on the faulting history.

BIC values show that the thermochronological data are best explained by a two-phase exhumation scenario with a proto-plateau on the mean elevation of  $\sim$ 5 km (Run C4). Results are reported in Figure 6, Figure S3 and Table S5 in Supporting Information S1. The best-fit model (misfit = 0.37) suggests that rapid exhumation initiated at  $\sim$ 12.00 Ma until 4.40 Ma with a rate of 2.10 mm/yr, followed by a second phase of slower exhumation (0.20 mm/yr) at 4.40–0 Ma. Both the scatter plots and unimodal marginal probability density functions supported the reliability of this inversion (Figure 6). Although the first-phase exhumation rate is variable, the scatter plot converges to a very small range at the concentrated value of the best-fit model (Figure 6b). Moreover, the onset time of the faulting on the profile CC' is similar to that of the profile DD', which is agreement with the fact that both profiles are geographically very close (Figure 2a). Thus, the inversion results of the profile CC' can reasonably represent the exhumation history.

## 5. Discussion

## 5.1. Activities of the Yadong Rift

Our updated interpretations of new and previously published thermochronology data reveal the activation history for the Yadong rift. The hanging wall of the Yadong rift experienced slow exhumation, as observed in profile BB' (Figure 4b). Conversely, the Yadong footwall rocks, best observed in profile CC', were rapidly exhumed at ~13–11 Ma with a rate of 0.9 mm/yr, documented by a series of BtAr ages (Gong et al., 2012; Xu et al., 2013; Figure 4c). Exhumation continued until ~5 Ma revealed by AHe and ZFT data (0.4–0.3 mm/yr; profile CC' and DD', Figures 4c and 4d).

Thermokinematic modeling on the profiles CC' and DD' revealed compatible results with those from AERs. PECUBE inversion suggests that the Yadong rifting began at  $\sim$ 12–11 Ma. This onset age estimate is consistent with the age marked by steep AER on the profile DD' and the BtAr data on the profile CC', whereas the modeled exhumation rates are faster than those obtained from the AERs. This is possibly due to the heat advection of the fault footwall rocks considered via thermokinematic modeling (e.g., Wolff et al., 2020).

The rate and magnitude of E-W extension along the Yadong rift can be estimated from the exhumation constraints. In the PECUBE model, the inverted slip rate ( $\sim$ 1.14 mm/yr) at the profile DD' corresponds to the extensional and exhumation components of  $\sim$ 0.73 mm/yr and  $\sim$ 0.87 mm/yr, assuming a 50° fault dip. This corresponds to  $\sim$ 8 km horizontal extension and  $\sim$ 9.6 km vertical exhumation since  $\sim$ 11 Ma. Similarly, the two-phase inverted rates at the profile CC' yield horizontal extensional components of  $\sim$ 1.35 mm/yr (12.00–4.40 Ma) and 0.13 mm/yr (4.40–0 Ma), respectively, which can be integrated to  $\sim$ 10.8 km horizontal extension and  $\sim$ 12.8 km vertical

BIAN ET AL. 11 of 23

10.1029/2021TC007091

exhumation. In addition, using the thermochronological dating, the extension rate on the profile CC' is calculated as  $\sim$ 2.0–0.8 mm/yr (13–5 Ma) based on the exhumation rate ( $\sim$ 2.4–0.9 mm/yr) obtained from the cooling history of the BtAr and AHe ages, which accommodates  $\sim$ 16–6.4 km horizontal extension. The above different calculation methods show consistent results.

## 5.2. Along-Strike Spatiotemporal Pattern for the North-Trending Rifts

#### 5.2.1. Constraints on the Initiation Timing

Rifting in southern Tibet is a lithospheric-scale event, which has been revealed by several observational data sets. First, tomographic images and receiver function images suggested that the Moho has been offset below major rifts (e.g., X. Y. Guo et al., 2018; Ren & Shen, 2008; Shi et al., 2015, 2016; Tian et al., 2015; Z. J. Zhang et al., 2013) and the low Pn velocity beneath the rifts provides evidence for the rifts cutting through the entire crust (Z. Guo et al., 2009; Nie et al., 2020). Second, earthquake focal mechanisms show brittle E-W extension in the mantle directly beneath the rifts (W. P. Chen & Kao, 1996; W. P. Chen & Yang, 2004). Third, major rifts across Tibet have wide spacing that suggests involvement of the mantle lithosphere (Yin, 2000). Forth, Helium in hot springs from upper mantle is observed in the Tibetan rift zones (Hoke et al., 2000). The lithospheric-scale rifting means that the "initiation" of regional extension could be manifested by a series of related processes, such as the ductile deformation at middle-lower-crust levels, rapid exhumation of footwall rocks of normal faults at the upper to middle-crustal level, and surface depressions accompanied by basin formation. Rifting may propagate very quickly from the lower-crustal level to the earth surface (Liao & Gerya, 2014; Pang et al., 2018). Therefore, we argue that although these processes happen at different structural levels, all of them are actually related to the initiation of rifting and could be used to constrain its timing (e.g., Cooper et al., 2015; Lee et al., 2011; Styron et al., 2011 and references therein). In general, previous studies document geochronology of syn-deformational fabrics to constrain ductile deformation events (e.g., Langille et al., 2012; Larson et al., 2020; J. J. Zhang & Guo, 2007), low-temperature thermochronology data that reveal rapid exhumation due to normal faulting (e.g., Dewane et al., 2006; Harrison et al., 1995; Hintersberger et al., 2010; Kali et al., 2010; J. L. D. Kapp et al., 2005; Lee et al., 2011; Mahéo et al., 2007; McCallister et al., 2014; Murphy et al., 2002; Styron et al., 2013; Sundell et al., 2013; Thiede et al., 2006; Wolff et al., 2019; Woodruff et al., 2013), or sediment ages via magnetostratigraphy to try to constrain the initial sedimentation of rift-related basins (e.g., Garzione et al., 2003, 2000; Ha et al., 2018; Saylor et al., 2010, 2009). Cross-cutting relationships (e.g., Cooper et al., 2015; Edwards & Harrison, 1997), magmatic dyke ages (Williams et al., 2001) and hydrothermal veins ages (Coleman & Hodges, 1995) can also provide additional constraints, although commonly as minimum or maximum initiation age constraints and not absolute values. Here, we objectively analyzed the constraint type of each study (Table S7 in Supporting Information S1), providing evaluation on how applicable the method is for constraining the initiation age of the local rift segment. In our compilation (Figure 7a; Table S7 in Supporting Information S1), we chose data sets that could be resolved initiation age of the rifts to compile the spatiotemporal distribution map of the rift initiation timing (Figure 1a). When different studies and methods disagree, we chose the oldest age constraint that reasonably documented extension, unless the data are questionable.

Our new constraints on the Yadong rift, the southern segment of the YGR, allow for a high-resolution examination of the along-strike variation in the initiation timing of the YGR when compared with published data sets on the central and northern segments. Our results illustrate that rifting initiated in the south and propagated northward along the strike of the YGR (Figure 1a). Specifically, rifting initiated in the south at  $\sim$ 13–11 Ma as recorded by the Yadong rift (this study) and before 10.8 Ma by the Gyanze rift (Ratschbacher et al., 2011), in the center at or before  $\sim$ 8.7–7 Ma as documented in the Ringbung and Nyainqentanghla ductile shear zone (Harrison et al., 1995; J. L. D. Kapp et al., 2005), and then in the north at  $\sim$ 7–5 Ma as revealed by thermochronology results in the Gulu rift (Stockli et al., 2002).

The other rifts across southern Tibet initiated nearly synchronously along strike, which is markedly different from the northward propagation trend of the YGR (Figures 1a and 7). Along the Gurla Mandhata (b in Figure 1a)-Lunggar rift (c and d in Figure 1a) system, monazite Th-Pb ages in syn-deformational leucogranites revealed ~15 Ma initiation for the Gurla Mandhata detachment fault zone (Murphy & Copeland, 2005). Moreover, PECUBE modeling based on ZHe data suggested that the South Lunggar rift (c in Figure 1a) initiated at 16–12 Ma (Styron et al., 2013). They are similar to the 15 Ma initiation in the North Lunggar rift (d in Figure 1a) observed by zircon U-Pb ages of syn-deformational leucogranites (P. Kapp et al., 2008). This nearly

BIAN ET AL. 12 of 23



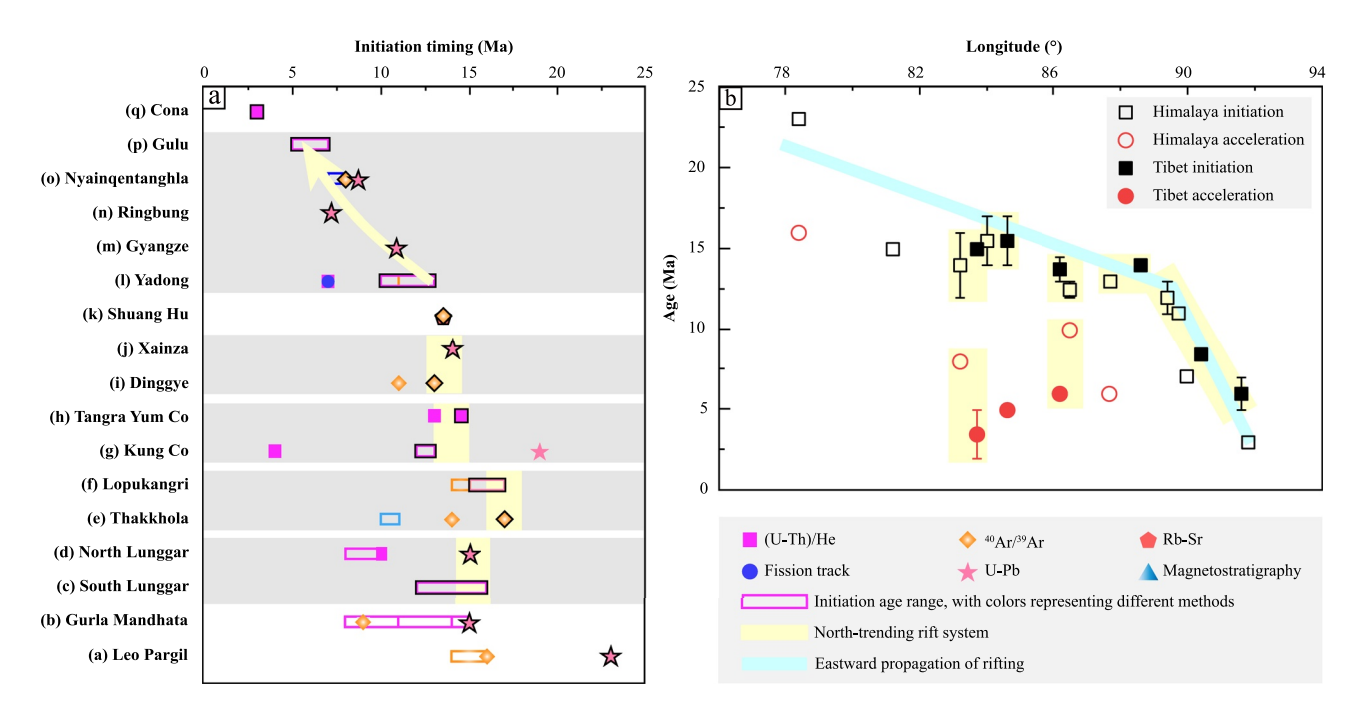


Figure 7. (a) Initiation timing estimates for north-trending rifts in the Himalayan-Tibetan system, with the same rift system incorporated in a gray box. Various shapes represent different methods to constrain the rift initiation timing. The rectangles denote the range of initiation timing estimates, where the colors represent different methods, consistent with the colors of the shapes. Data sets outlined with black lines are interpreted to the best representative of the initiation age of an individual rift system (Figure 1a). (b) Longitudinal variations in the initiation and acceleration timing for north-trending rifts, with the same rift system incorporated in a gray box. Initiation timing of Yadong-Gulu rift (YGR) youngs northward, but each rift system to its west initiated nearly coevally along strike within the error range of 2 Myr. Acceleration timing of the rifts west of the YGR is broadly later in the Lhasa terrane than that in the Himalaya, revealing that they experienced northward younging acceleration along strike. Detailed data and references are in Table S7 in Supporting Information S1.

synchronous initiation is also observed by the reconstruction in extension history along the Lunggar rift (Styron et al., 2015). Along the Thakkhola (e in Figure 1a)-Lopukangri (f in Figure 1a) rift system, the onset of the both rifts was constrained at ~17–14 Ma by muscovite  $^{40}$ Ar/ $^{39}$ Ar thermochronology for the Thakkhola graben (Coleman & Hodges, 1995; Larson et al., 2020) and by zircon U-Pb geochronology and mica  $^{40}$ Ar/ $^{39}$ Ar thermochronology for the Lopukangri rift (Laskowski et al., 2017; Sanchez et al., 2010), respectively. To the east, the other two rift systems also present a broad simultaneous pattern along their strikes. For example, along the Kung Co (g in Figure 1a)-Tangra Yum Co (h in Figure 1a) rift system, ZHe and AHe data revealed that the initiation timing was constrained at ~13–12 Ma for the Kung Co rift (Lee et al., 2011) and 14.5–13 Ma for the Tangra Yum Co (Dewane et al., 2006; Wolff et al., 2019), respectively. Similarly, along the Dinggye (i in Figure 1a)-Xainza (j in Figure 1a) rift system, the Dinggye rift started to activate at ~13–12 Ma as constrained by BtAr thermochronology from syn-deformational rocks (Kali et al., 2010; J. J. Zhang & Guo, 2007), and the Xainza rift initiated at ~14 Ma based on ZHe and AHe data (Hager et al., 2009; Sundell et al., 2013).

In general, initiation timing constraints for each rift system west of the YGR show negligible variations along strike, and thus they each may be considered to have initiated synchronously along strike. The northward younging trend of rift initiation along strike of the YGR is therefore unique in southern Tibet.

## 5.2.2. Acceleration Timing

Rift acceleration is defined here as either a marked increase in extension-related exhumation rates or as renewed exhumation after an apparent lull. Along the Lunggar rift (c and d in Figure 1a), rift acceleration was documented by AHe and ZHe data, with acceleration younging northward from  $\sim$ 8 Ma in the South Lunggar rift to  $\sim$ 5–2 Ma in the North Lunggar rift (Styron et al., 2015, 2013; Sundell et al., 2013). Along the Kung Co-Tangra Yum Co rift (g and h in Figure 1a), the acceleration timing of the Kung Co rift was constrained at  $\sim$ 10 Ma with a high rate of 19–6 mm/yr inferred by inverse modeling of ZHe and AHe data (Lee et al., 2011), which is earlier than a dominant pulse of rifting at  $\sim$ 6 Ma in the Tangra Yum Co rift (Dewane et al., 2006). In addition, several sporadic acceleration timings were recorded in the Leo Pargil detachment zone (a in Figure 1a,  $\sim$ 16 Ma, Langille

BIAN ET AL. 13 of 23



et al., 2012; Thiede et al., 2006), Lopukangri rift (f in Figure 1a, <5 Ma, Sanchez et al., 2010), and Dinggye rift (i in Figure 1a, ~6 Ma, Kali et al., 2010), showing broadly younger timing of rift acceleration in the Lhasa terrane than in the Himalaya (Sundell et al., 2013). In general, available data show that rifts west of the YGR experienced northward younging in rift acceleration (Figure 7b).

## 5.3. Evaluation of E-W Extension Models

Numerous models have been proposed to explain E-W extension in the Himalayan-Tibetan orogen, including convective thinning of lithospheric mantle (England & Houseman, 1989), gravitational collapse (Molnar & Tapponnier, 1978), radial spreading (Seeber & Armbruster, 1984) or oroclinal bending (Klootwijk et al., 1985) of the Himalayan arc, oblique convergence of the Indian continent (McCaffrey & Nabelek, 1998), tearing (Yin, 2000) or lateral detachment (Webb et al., 2017) of the Indian slab and eastward flow of lithosphere (Yin & Taylor, 2011). Most of these models predict distinct spatiotemporal patterns of rifting (e.g., McCallister et al., 2014; Styron et al., 2011), and thus the trend of rift initiation timing becomes a critical test to evaluate proposed hypotheses (e.g., Bian, Gong, Zuza, et al., 2020). Recently, Bian, Gong, Zuza, et al. (2020) demonstrated a general pattern of both eastward younging rifting and decreasing rift-extension magnitudes. Based on these observations, Bian, Gong, Zuza, et al. (2020) proposed that regional E-W extension is related to eastward lateral slab detachment and resultant establishment of gravitational potential energy gradients (Lechmann et al., 2014; Y. Q. Yang & Liu, 2013) that drove eastward lithospheric flow (e.g., Bischoff & Flesch, 2018; Yin & Taylor, 2011; Z. J. Zhang et al., 2013). This model reasonably explains the spatiotemporal patterns of rifting in the E-W direction.

However, the along-strike variation of rift development remains obscure, specifically along individual rift systems, which previously prohibited testing of models that emphasized north-south variations in rift initiation. For example, the radial spreading model suggests that the Himalayan arc expanded outward as south-directed thrusts in the Himalayas initiated successively toward the foreland (DeCelles et al., 2001; Haproff et al., 2018; Molnar & Lyon-Caent, 1989; Murphy & Copeland, 2005; Murphy et al., 2009; Seeber & Armbruster, 1984; Seeber & Pêcher, 1998), which predicts a southward along-strike propagation of rift initiation ages. Alternatively, the oblique convergence model interprets E-W extension based on the increasing arc-parallel component of the convergence vectors between the Indian slab and the Himalayan arc toward the eastern and western Himalaya (M. Liu & Yang, 2003; McCaffrey & Nabelek, 1998; McCallister et al., 2014; Styron et al., 2011), which predicts a northward propagation trend of rift initiation. However, these two models both require that rift initiation is synchronous across strike, or youngs toward the center, which is inconstant with the observation of a monotonic eastward rifting pattern discussed above. The other two rifting models (i.e., longitudinal slab tearing and underthrusting) do not have a generic rift initiation pattern in the E-W direction, but they do predict that rifting should follow or parallel activities of the subducting/underthrusting slab. That is, rifting will follow the same major patterns of the Indian slab, such as diachronous underthrusting or variable E-W initiation of longitudinal slab tearing.

On the one hand, the longitudinal slab tearing model (Y. Chen et al., 2015; Duan et al., 2017; J. T. Li & Song, 2018; Z. Liu et al., 2020; Pei et al., 2016; Si et al., 2019; G. Wang et al., 2017; C. L. Wu et al., 2019; Xiao et al., 2007; Yin, 2000) predicts that rift initiation should propagate southward in response to the tearing of the Indian slab from north to south. The southward slab tearing has been supported by several lines of evidence. Post-collisional ultrapotassic rocks along the north-trending rifts, particularly in Tangra Yum Co rift (Figure 1a, Z. F. Guo et al., 2013), show a southward younging trend, which is interpreted as a representative for the southward lithospheric tear (Ding et al., 2006; X. Y. Guo et al., 2018; Z. F. Guo & Wilson, 2019; Hou et al., 2006; R. Wang et al., 2021; Yan et al., 2019). This scenario is analogous to slab tearing that has been postulated worldwide, such as in Turkey (Dilek & Altunkaynak, 2009; Govers & Fichtner, 2016), Indonesia (Koulakov et al., 2016), Japan (Obayashi et al., 2009), Italy (Gutscher et al., 2016), Mariana (Miller et al., 2006) and South America (Hu & Liu, 2016). In all these cases, slab tear propagates inward from the tip of subducting slab. In addition, numerical simulations suggested that the subducting slab would first undergo lateral detachment and then turn into the longitudinal tearing (Z. H. Li et al., 2013; Sternai et al., 2014). In this process, the slab tearing was initiated at the slab tip and migrated toward the subduction-upper plate interface.

Alternatively, the slab underthrusting model suggests that the northward insertion of the Indian slab drives surface rifting (DeCelles et al., 2002; Lee et al., 2011; Styron et al., 2015; Sundell et al., 2013), thus predicting a north-

BIAN ET AL. 14 of 23



ward propagation of initiation or acceleration of individual rift systems. Styron et al. (2015) demonstrated that northward acceleration of E-W rifting along the Lunggar rift (Figure 1a) correlated with the northward propagation of the underthrusting Indian slab front. To test this model, here we conducted 2D thermo-mechanical simulations (Figure S4 in Supporting Information S1) adopting the I2VIS code (Gerya & Yuen, 2003) to investigate the slab underthrusting process (Section S1 in Supporting Information S1). Results suggest that the Indian slab began to underthrust northward after slab detachment, which significantly increases upper-plate compressional stress and favors the strong coupling with the overlying plate (Figure S5 in Supporting Information S1, e.g., Bian, Gong, Chen, et al., 2020; Genge et al., 2021; L. Li, Murphy, et al., 2020; S. H. Li, van Hinsbergen, et al., 2020). This process could thicken the Tibetan crust by ~30 km to reach ~80 km thickness (Figure S6a in Supporting Information S1), which related topographic uplift to elevations >4 km (Figure S6b in Supporting Information S1). Assuming the crustal column is at peak thickness and body forces matches plate-boundary stresses, lower crustal thickening may be balanced by mid-upper crustal thinning by accelerated rifting.

The along-strike variations in the timing of rift initiation or acceleration provide crucial constraints to evaluate two above-mentioned models. As has been summarized above, the YGR propagated northward while most rifts to the west initiated nearly synchronously along their strikes. We argue that all these rift-initiation trends are at odds with predictions of both the slab tearing and slab underthrusting models. Nevertheless, post-initiation acceleration events present a northward propagation pattern, such as documented in the Lunggar rift (c and d in Figure 1a; Styron et al., 2015) and the Kung Co-Tangra Yum Co rift system (g and h in Figure 1a; Dewane et al., 2006; Lee et al., 2011; Wolff et al., 2019).

It is noteworthy that the YGR contrasts with the other rift systems to its west in the along-strike pattern of rift initiation. This implies that the YGR may express a slightly different tectonic scenario. Furthermore, although the nearly along-strike synchronous initiation of rift systems west of the YGR do not appear to be significantly affected by slab northward underthrusting, their late-stage rifting acceleration was (e.g., Lee et al., 2011; Styron et al., 2015, 2013; Sundell et al., 2013). Therefore, some tectonic "switch" is required to cause underthrusting to transition from negligible influence on rift initiation to an appreciable impact on rift acceleration. Reasonable working hypotheses should explain these observations, such as one we propose in the following section.

# 5.4. Working Hypothesis

We propose an updated working hypothesis for E-W extension, which uniquely evaluates potential geodynamic process in the N-S direction based on the newly revealed northward rift-initiation for the YGR. This hypothesis proposes that both slab longitudinal tearing and underthrusting had a minimal impact on rift initiation, with the detailed process described as follows. During the initial lateral slab detachment process (Figure 8a), the subducting Indian slab, following slab rollback, was anchored in the mantle with a relatively steep dip angle (DeCelles et al., 2011; Leary et al., 2016; Replumaz et al., 2010), which resulted in negligible effects on the initiation of north-trending rifts. Instead, rift initiation was primarily controlled by lateral slab detachment from the west and corresponding eastward lithospheric flow (Figure 8a; Bian, Gong, Zuza, et al., 2020; Webb et al., 2017). Individual rift systems initiated approximately simultaneously along strike due to uniform lithospheric flow.

Eastward propagation of lateral slab detachment also produced longitudinal tearing, causing rebound of the released slab and a shallower subducting angle (Figures 8b and 8c). This proposal is consistent with geophysical observations that the dip angle of the Indian lithospheric slab becomes steeper while the horizontal sliding distance to the north becomes shorter from west to east (Y. Chen et al., 2015; Kind & Yuan, 2010; Kosarev et al., 1999; C. Li et al., 2008; L. Li, Murphy, et al., 2020; S. H. Li, van Hinsbergen, et al., 2020; Nabelek et al., 2009; Priestley et al., 2006; Zhao et al., 2010; Zhou & Murphy, 2005). The flattened Indian slab began to underthrust northward as India-Asia plate convergence continued (Figure 8b), which induced a second stage of northward propagating extensional acceleration across many of the rifts west of the YGR (Figures 8b and 8c; Lee et al., 2011; Styron et al., 2015; Sundell et al., 2013). This process explains why rifts west of YGR initiated almost synchronously along their strikes but display a northward younging trend in the later stage of accelerated extension (Styron et al., 2015; Sundell et al., 2013). The insertion of India into Asia during underthrusting also helped to balance crustal thickness during regional extension, such that crustal thickness did not thin significantly during this time since the middle Miocene (e.g., Sundell et al., 2021).

BIAN ET AL. 15 of 23



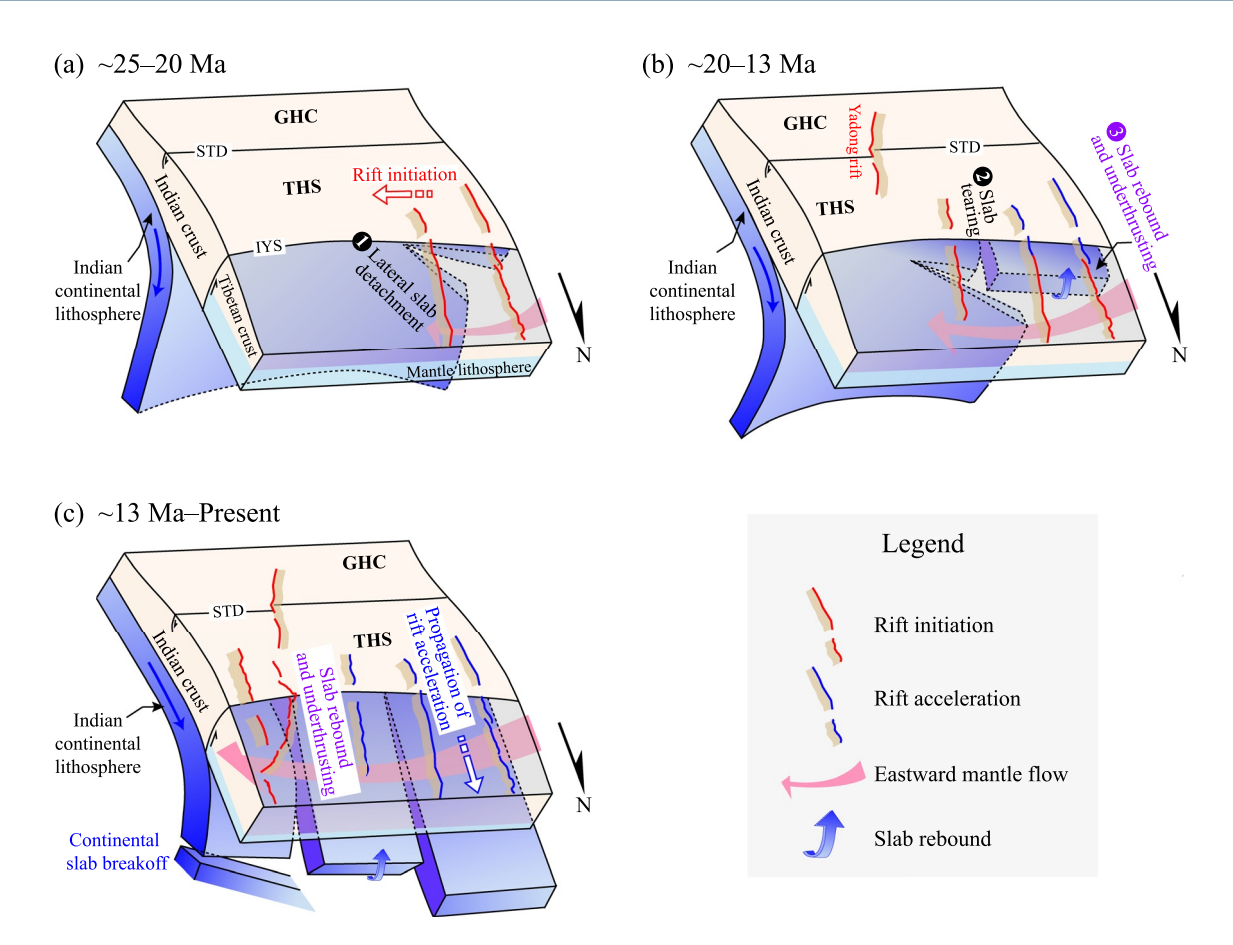


Figure 8. Schematic diagrams of geodynamic processes for E-W extension. (a)  $\sim$ 25–20 Ma: lateral slab detachment and related eastward lithospheric flow drove eastward development of the rifting, while the subducting Indian slab with a steep-dip angle plays negligible effects on the initiation of north-trending rifts. (b)  $\sim$ 20–13 Ma: continued lateral slab detachment led to southward tearing, gentling the subducting angle and initiating underthrusting of the remaining slab, which induced the northward propagation of rift acceleration. The Yadong rift began to initiate due to slab detachment from the west, whereas Nyainqentanghla and Gulu rifts had not because slab detachment has not arrived yet. (c)  $\sim$ 13 Ma—present: continued lithospheric flow caused the eastward development of rift initiation, causing sequential initiation of the Nyainqentanghla, Gulu, and Cona rifts. At the same time, underthrusting of the western slabs released by tearing induced northward propagation of rift acceleration. Key to symbols: STD, South Tibet Detachment; IYS, Indus-Yarlung suture zone; GHC, Greater Himalayan Crystalline Complex; THS, Tethyan Himalayan Sequence.

However, the initiation of the Yadong rift and geodynamics for the YGR are different from the rift systems to the west, which may be due to its specific geological features and location. In fact, the YGR is the longest rift system across Tibet and the most oblique one relative to the Himalayan arc, striking northeast from longitude ~89°E to ~91.7°E (Figure 1a). We propose that its specific strike with a broad lateral longitudinal span may result in the observed northward younging trend in rift initiation timing (from 13-11 to 7-5 Ma) within the background of eastward younging initiation trend, such that the southern Yadong rift is located in the west whereas the northern Gulu rift is farther east. The reason why the YGR presents a unique strike compared with other rift systems may beyond the scope of this study, but we consider that this could be induced by stress heterogeneity (e.g., Manighetti et al., 2015) focused along its unique spatial and tectonic location. Across the YGR from west to east, the (a) Indian slab subducted with an abruptly steeper angle (J. T. Li & Song, 2018; Liang et al., 2016; Shi et al., 2015, 2016; G. Wang et al., 2017), (b) Himalayan arc presents asymmetric curvatures (Bendick & Bilham, 2001; Webb et al., 2017), (c) present-day global positioning system velocity field data show obvious transition, from NNE-directed to NE-directed vectors (Antolín et al., 2012; Gan et al., 2007; Q. Wang et al., 2001; S. G. Wang & Shen, 2020; Zheng et al., 2017), and (d) strike-slip domains change from left-lateral slip to right-lateral slip (Gan et al., 2007). If this proposal is correct, laterally migrating slab detachment would first arrive at the position below the Yadong rift, causing its activation at 13-11 Ma, and then propagate to the Nyaingentanghla, causing rifting at ~8 Ma (Figure 8c, Harrison et al., 1995).

BIAN ET AL. 16 of 23



The special background of the YGR is also outstanding in the transition in rifting propagation rate. Our integrated data sets demonstrate that extension initiation migrated eastward across southern Tibet rapidly from Leo Pargil to Yadong rift at a rate of ~1.3 longitudinal degrees per million year, which then slowed to an eastward migration rate of ~0.3 longitudinal degrees per million year from Yadong to Cona (Figure 1b). It is noteworthy that the eastward development of post-collisional magmatic activities also slowed down when passing the Yadong rift, from ~3 longitudinal degrees per million year at the west to ~0.5 at the east (Figure 1b). Subsequently, continued eastward slab detachment and lithospheric flow led to the initiation of the Cona rift system to the east of the YGR (Figure 8c). The Cona rift exhibits no significant late-stage acceleration (Bian, Gong, Zuza, et al., 2020), possibly because the subducting Indian slab remains at a steep dip angle there and underthrusting is not yet active. We argue that this kinematic history and rift vs. magmatism correlation support our model of coupled lateral slab detachment and eastward lithospheric flow, possibly implying a slowdown of these processes as they migrate eastward. The slowing of eastward rift migration may reflect (a) proximity to the Eastern Himalaya Syntaxis, which tilted southern Tibet westward to expose granulite grade rocks relative to shallow crustal rocks exposed near Lhasa (e.g., Cao et al., 2020) or (b) interaction between the Indian slab and the north-trending Eastern Flanking belts (e.g., Haproff et al., 2020).

Alternatively, the Yadong rift is spatially located south of the STD in the GHC of the Himalaya (Figure 1a), at the longitude where Himalayan arc curvature changes abruptly (e.g., Bendick & Bilham, 2001; Webb et al., 2017). Therefore, it is possible that the earlier initiation of the Yadong rift in the context of the YGR may be uniquely affected by outward expansion of the Himalayan arc due to the southward propagation of east-trending thrusts (e.g., Fan & Murphy, 2021; Murphy & Copeland, 2005; Murphy et al., 2009). This local impact may emphasize aspects of the working hypothesis described above.

In summary, we argue that eastward slab detachment caused both lithospheric flow and longitudinal slab tearing, the former of which controlled the initiation of north-trending rifts. Slab tearing did not actually drive the initiation of crustal rifting toward south, but rather acted as a switch, activating the effects by Indian slab underthrusting that drove a northward trend of rift acceleration to balance northward propagating lower crustal thickening. Furthermore, along the YGR, the observed northward younging initiation trend could be attributed to its orientation of the most oblique northeast-trend, and/or locally outward expansion of the Himalayan arc that potentially induced the earlier activation of the Yadong rift, the southernmost segment of the YGR. The updated working hypothesis reasonably explains the observed along-strike spatiotemporal patterns of rifting and magmatism. This model reevaluates the roles of the slab underthrusting and tearing on intra-orogen rift development. Further evaluation of this working hypothesis will benefit from future studies that provide updated constraints on along-strike rift initiation and kinematics.

## 6. Conclusions

Thermochronological data reasonably constrained the activation history of the Yadong rift. Both the age-elevation profiles and thermokinematic modeling (PECUBE) suggest that the rifting initiated at  $\sim$ 13–11 Ma with a slip rate of  $\sim$ 1 mm/yr. The integration of published data and our new results reveal that the initiation age along strike of the YGR youngs from south to north. In addition, each rift system to the west of the YGR initiated nearly synchronously along strike but displays a northward younging trend in the later rift acceleration stages. These observations contrast with the predictions of the slab tearing model that requires a southward younging trend of rift initiation. Our updated working hypothesis highlights that slab tearing allowed slab underthrusting to take effect, causing rifting to accelerate northward. The unique northward younging initiation along the YGR could be associated with its orientation of the most oblique northeast-trending and/or outward expansion of the Himalayan arc.

# **Data Availability Statement**

The data set adopted in this paper can be accessed at National Tibetan Plateau Data Center (http://data.tpdc.ac.cn/zh-hans/data/17a62185-3bb2-4431-9279-dfd57643c54e/).

BIAN ET AL. 17 of 23



## Acknowledgments

This research is supported by the National Natural Science Foundation of China (Nos. 41941016, 41472182, and 41720104003), Basic public welfare research project of Zhejiang Province (No. LY21D020002), the Basic Science Centre Programme for Multiphase Media Evolution in Hypergravity of the National Natural Science Foundation of China (No. 51988101), the Second Tibetan Plateau Scientific Expedition and Research (STEP) (No. 2019QZKK0708), the National S&T Major Project (Grant Nos. 2017ZX05008-001, 2017ZX05003-001) and the NSF Tectonics Program (No. 1914501). Field work was assisted by Drs. Kaixuan An, Dongxu Chen and Chentao Zhu and Mr. Linshen Chen. The authors appreciate the handling of the Editor Taylor Schildgen and the Associate Editor. We benefited greatly from the constructive comments from two anonymous reviewers.

## References

- Akaike, H. (1974). A new look at the statistical model identification. *IEEE Transactions on Automatic Control*, 19(6), 716–723. https://doi.org/10.1109/tac.1974.1100705
- Antolín, B., Schill, E., Grujic, D., Baule, S., Quidelleur, X., Appel, E., & Waldhör, M. (2012). E-W extension and block rotation of the southeastern Tibet: Untraveling late deformation stages in the Eastern Himalaya (NW Bhutan) by means of pyrrhotite remanences. *Journal of Structural Geology*, 42, 19–33. https://doi.org/10.1016/j.jsg.2012.07.003
- Armijo, R., Tapponnier, P., Mercier, J. L., & Han, T. L. (1986). Quaternary extension in southern Tibet: Field observations and tectonic implications. *Journal of Geophysical Research: Solid Earth*, 91(B14), 13803–13872. https://doi.org/10.1029/JB091iB14p13803
- Bendick, R., & Bilham, R. (2001). How perfect is the Himalayan arc? *Geology*, 29, 791–794. https://doi.org/10.1130/0091-7613(2001) 029<0791:hpitha>2.0.co;2
- Bian, S., Gong, J. F., Chen, L., Zuza, A. V., Chen, H. L., Lin, X. B., et al. (2020). Diachronous uplift in intra-continental orogeny: 2D thermo-mechanical modeling of the India-Asia collision. *Tectonophysics*, 775, 228310. https://doi.org/10.1016/j.tecto.2019.228310
- Bian, S., Gong, J. F., Zuza, A. V., Yang, R., Tian, Y. T., Ji, J. Q., et al. (2020). Late Pliocene onset of the Cona rift, Eastern Himalaya, confirms east-ward propagation of extension in Himalayan-Tibetan orogen. *Earth and Planetary Science Letters*, 544(15), 116383. https://doi.org/10.1016/j.epsl.2020.116383
- Bischoff, S. H., & Flesch, L. M. (2018). Normal faulting and viscous buckling in the Tibetan Plateau induced by a weak lower crust. *Nature Communications*. 9, 4952. https://doi.org/10.1038/s41467-018-07312-9
- Blisniuk, P. M., Hacker, B. R., Glodny, J., Ratschbacher, L., Bi, S. W., Wu, Z. H., et al. (2001). Normal faulting in central Tibet since at least 13.5 Myr ago. *Nature*, 412, 628–632. https://doi.org/10.1038/35088045
- Braun, J. (2002). Quantifying the effect of recent relief changes on age-elevation relationships. *Earth and Planetary Science Letters*, 200, 331–343. https://doi.org/10.1016/S0012-821X(02)00638-6
- Braun, J. (2003). Pecube: A new finite-element code to solve the 3-D heat transport equation including the effects of a time-varying, finite amplitude surface topography. *Computers and Geosciences*, 29(6), 787–794. https://doi.org/10.1016/S0098-3004(03)00052-9
- Braun, J., van der Beek, P., & Batt, G. E. (2006). Quantitative thermochronology. Cambridge, UK: Cambridge University Press.
- Braun, J., van der Beek, P., Valla, P., Robert, X., Herman, F., Glotzbach, C., et al. (2012). Quantifying rates of landscape evolution and tectonic processes by thermochronology and numerical modeling of crustal heat transport using PECUBE. *Tectonophysics*, 524–525(1), 1–28. https://doi.org/10.1016/j.tecto.2011.12.035
- Burchfiel, B. C., Chen, Z., Hodges, K. V., Liu, Y., Royden, L. H., Deng, C., & Jiene, X. (1992). The South Tibetan detachment system, Himalayan orogen: Extension contemporaneous with and parallel to shortening in a collisional mountain belt. *Geological Society of America, Special Papers*, 269, 1–41. https://doi.org/10.1130/SPE269-p1
- Burchfiel, B. C., Deng, Q. D., Molnar, P., Royden, L., Wang, Y. P., Zhang, P. Z., et al. (1989). Intracrustal detachment within zones of continental deformation. *Geology*, 17, 448–452. https://doi.org/10.1130/0091-7613(1989)017<0448:IDWZOC>2.3.CO;2
- Campani, M., Herman, F., & Mancktelow, N. (2010). Two- and three-dimensional thermal modeling of a low-angle detachment: Exhumation history of the Simplon Fault Zone, central Alps. *Journal of Geophysical Research: Solid Earth*, 115(B10), B10420. https://doi.org/10.1029/2009JB007036
- Cao, W. R., Yang, J. M., Zuza, A. V., Ji, W. Q., Ma, X. X., Chu, X., & Burgess, Q. P. (2020). Crustal tilting and differential exhumation of Gangdese Batholith in southern Tibet revealed by bedrock pressures. Earth and Planetary Science Letters, 543, 116347. https://doi. org/10.1016/j.epsl.2020.116347
- Carrapa, B., Robert, X., DeCelles, P. G., Orme, D. A., Thomson, S. N., & Schoenbohm, L. M. (2016). Asymmetric exhumation of the Mount Everest region: Implications for the tectono-topographic evolution of the Himalaya. *Geology*, 44(8), 611–614. https://doi.org/10.1130/G37756.1
- Chen, S. Y., Zhang, B., Zhang, J. J., Wang, Y., Li, X. R., Zhang, L., et al. (2022). Tectonic transformation from orogen-perpendicular to orogen-parallel extension in the North Himalayan Gneiss Domes: Evidence from a structural, kinematic, and geochronological investigation of the Ramba gneiss dome. *Journal of Structural Geology*, 155, 104527. https://doi.org/10.1016/j.jsg.2022.104527
- Chen, W. P., & Kao, H. (1996). Seismotectonics of Asia: Some recent progress. In A. Yin, & T. M. Harrison (Eds.), *The tectonic evolution of Asia* (pp. 37–52). Cambridge, UK: Cambridge University Press.
- Chen, W. P., & Yang, Z. (2004). Earthquakes beneath the Himalayas and Tibet: Evidence for strong lithospheric mantle. *Science*, 304(5679), 1949–1952. https://doi.org/10.1126/science.1097324
- Chen, Y., Li, W., Yuan, X., Badal, J., & Teng, J. (2015). Tearing of the Indian lithospheric slab beneath southern Tibet revealed by SKS-wave splitting measurements. Earth and Planetary Science Letters, 413, 13–24. https://doi.org/10.1016/j.epsl.2014.12.041
- Chevalier, M. L., Tapponnier, P., van der Woerd, J., Leloup, P. H., Wang, S., Pan, J., et al. (2020). Late Quaternary extension rates across the northern half of the Yadong-Gulu rift: Implication for east-west extension in southern Tibet. *Journal of Geophysical Research: Solid Earth*, 125, e2019JB019106. https://doi.org/10.1029/2019JB019106
- China University of Geosciences. (2002). Report of Regional Geological Survey of P. R. China, Yadong County (1:250,000). China Geological Survey Special Publication No. G45C001004.
- Coleman, M., & Hodges, K. (1995). Evidence for Tibetan plateau uplift before 14 Myr ago from a new minimum age for east-west extension. Nature, 374, 49–52. https://doi.org/10.1038/374049a0
- Cooper, F. J., Hodges, K. V., Parrish, R. R., Roberts, N. M. W., & Horstwood, M. S. A. (2015). Synchronous N-S and E-W extension at the Tibet-to-Himalaya transition in NW Bhutan. *Tectonics*, 34, 1–1395. https://doi.org/10.1002/2014TC003712
- Copley, A., Avouac, J. P., & Wernicke, B. P. (2011). Evidence for mechanical coupling and strong Indian lower crust beneath southern Tibet. Nature, 472(7341), 79–81. https://doi.org/10.1038/nature09926
- Dai, J. G., Fox, M., Han, X., Tremblay, M. M., Xu, S. Y., Shuster, D. L., et al. (2021). Two stages of accelerated exhumation in the middle reach of the Yarlung River, southern Tibet since the mid-Miocene. *Tectonics*, 40(6), e2020TC006618. https://doi.org/10.1029/2020TC006618
- DeCelles, P. G., Kapp, P., Quade, J., & Gehrels, G. E. (2011). Oligocene-Miocene Kailas basin, southwestern Tibet: Record of postcollisional upper-plate extension in the Indus-Yarlung suture zone. *The Geological Society of America Bulletin*, 123(7–8), 1337–1362. https://doi.org/10.1130/b30258.1
- DeCelles, P. G., Robinson, D. M., Quade, J., Ojha, T. P., Garzione, C. N., Copeland, P., & Upreti, B. N. (2001). Stratigraphy, structure, and tectonic evolution of the Himalayan fold-thrust belt in western Nepal. *Tectonics*, 20, 487–509. https://doi.org/10.1029/2000tc001226
- Decelles, P. G., Robinson, D. M., & Zandt, G. (2002). Implications of shortening in the Himalayan fold-thrust belt for uplift of the Tibetan Plateau. *Tectonics*, 21(6), 12-1–12-25. https://doi.org/10.1029/2001TC001322
- Dewane, T. J., Stockli, D. F., Hager, C., & Taylor, M. H. (2006). Timing of Cenozoic E-W extension in the Tangra Yum Co-Kung Co rift, south-central Tibet. *American Geophysical Union fall Metting, abstract with program.*

BIAN ET AL. 18 of 23



- Dilek, Y., & Altunkaynak, Ş. (2009). Geochemical and temporal evolution of Cenozoic magmatism in western Turkey: Mantle response to collision, slab break-off, and lithospheric tearing in an orogenic belt. Geological Society, London, Special Publications, 311(1), 213–233. https://doi.org/10.1144/SP311.8
- Ding, L., Yue, Y. H., Cai, F. L., Xu, X. X., Zhang, Q. H., & Lai, Q. Z. (2006). 40 Arr/39 Ar geochronology, geochemical and Sr-Nd-O isotopic characteristics of the high-Mg ultrapotassic rocks in Lhasa block of Tibet: Implications in the onset time and depth of NS-striking rift system. *Acta Geological Sinica*, 80, 1252–1261.
- Dong, H. W., Larson, K. P., Kellett, D. A., Xu, Z. Q., Li, G. W., Cao, H., et al. (2020). Timing of slip across the South Tibetan Detachment system and Yadong-Gulu graben, Eastern Himalaya. *Journal of the Geological Society*, 178, 1–197. https://doi.org/10.1144/jgs2019-197
- Duan, Y. H., Tian, X. B., Liang, X. F., Li, W., Wu, C. L., Zhou, B. B., & Iqbal, J. (2017). Subduction of the Indian slab into the mantle transition zone revealed by receiver functions. *Tectonophysics*, 702, 61–69. https://doi.org/10.1016/j.tecto.2017.02.025
- Edwards, M. A., & Harrison, T. M. (1997). When did the roof collapse? Late Miocene north-south extension in the High Himalaya revealed by Th-Pb monazite dating of the Khula Kangri granite. *Geology*, 25, 543–546. https://doi.org/10.1130/0091-7613(1997)025<0543: wdtrcl>2.3.co:2
- England, P., & Houseman, G. (1989). Extension during continental convergence, with application to the Tibetan Plateau. *Journal of Geophysical Research: Solid Earth*, 94(B12), 17561–17579. https://doi.org/10.1029/JB094iB12p17561
- Fadil, A., Vernant, P., Mcclusky, S., Reilinger, R., Gomez, F., Sari, D. B., et al. (2006). Active tectonics of the western Mediterranean: Geodetic evidence for rollback of a delaminated subcontinental lithospheric slab beneath the Rif Mountains, Morocco. Geology, 34(7), 529–532. https://doi.org/10.1130/G22291.1
- Fan, S. Y., & Murphy, M. A. (2021). Three-dimensional strain accumulation and partitioning in an arcuate orogenic wedge: An example from the Himalaya. The Geological Society of America Bulletin, 133(1-2), 3-18. https://doi.org/10.1130/b35528.1
- Francheteau, J., Jaupart, C., Shen, X. J., Kang, W. H., Lee, D. L., Bai, J. C., et al. (1984). High heat flow in southern Tibet. *Nature*, 307, 32–36. https://doi.org/10.1038/307032a0
- Galbraith, R. F., & Green, P. F. (1990). Estimating the component ages in a finite mixture. International Journal of Radiation Applications and Instrumentation—Part D: Nuclear Tracks and Radiation Measurements, 17(3), 197–206. https://doi.org/10.1016/1359-0189(90)90035-V
- Gan, W. J., Zhang, P. Z., Shen, Z. K., Niu, Z. J., Wang, M., Wan, Y. G., et al. (2007). Present-day crustal motion within the Tibetan Plateau inferred from GPS measurements. *Journal of Geophysical Research: Solid Earth*, 112, B08416. https://doi.org/10.1029/2005JB004120
- Garzione, C. N., DeCelles, P. G., Hodkinson, D. G., Ojha, T. P., & Upreti, B. N. (2003). East-west extension and Miocene environmental change in the southern Tibetan Plateau, Thakkhola graben, central Nepal. *The Geological Society of America Bulletin*, 115, 3–20. https://doi.org/10.1130/0016-7606(2003)115<0003:eweame>2.0.co;2
- Garzione, C. N., Dettman, D. L., Quade, J., DeCelles, P. G., & Butler, R. F. (2000). High times on the Tibetan Plateau: Paleoelevation of the Thakkhola graben, Nepal. *Geology*, 28, 339–342. https://doi.org/10.1130/0091-7613(2000)028<0339:htottp>2.3.co;2
- Genge, M. C., Zattin, M., Savignano, E., Franchini, M., Gautheron, C., Ramos, V. A., & Mazzoli, S. (2021). The role of slab geometry in the exhumation of cordilleran-type orogens and their forelands: Insights from northern Patagonia. *The Geological Society of America Bulletin*, 133, 2535–2548. https://doi.org/10.1130/B35767.1
- Gerya, T. V., & Yuen, D. A. (2003). Characteristics-based marker-in-cell method with conservative finite-differences schemes for modeling geological flows with strongly variable transport properties. *Physics of the Earth and Planetary Interiors*, 140(4), 293–318. https://doi. org/10.1016/j.pepi.2003.09.006
- Glotzbach, C., Reinecker, J., Danišík, M., Rahn, M., Frisch, W., & Spiegel, C. (2008). Neogene exhumation history of the Mont Blanc massif, Western Alps. *Tectonics*, 27, 4177. https://doi.org/10.1029/2008TC002257
- Glotzbach, C., van der Beek, P. A., & Spiegel, C. (2011). Episodic exhumation and relief growth in the Mont Blanc massif, Western Alps from numerical modeling of thermochronology data. *Earth and Planetary Science Letters*, 304(3–4), 417–430. https://doi.org/10.1016/j.epsl.2011.02.020
- Gong, J. F., Ji, J. Q., Han, B. F., Chen, J. J., Sun, D. X., Li, B. L., et al. (2012). Early subduction-exhumation and late channel flow of the Greater Himalayan sequence: Implications from the Yadong section in the Eastern Himalaya. *International Geology Review*, 54(10), 1184–1202. https://doi.org/10.1080/00206814.2011.626604
- Govers, R., & Fichtner, A. (2016). Signature of slab fragmentation beneath Anatolia from full-waveform tomography. *Earth and Planetary Science Letters*, 450, 10–19. https://doi.org/10.1016/j.epsl.2016.06.014
- Guenthner, W. R., Reiners, P. W., Ketcham, R. A., Nasdala, L., & Giester, G. (2013). Helium diffusion in natural zircon: Radiation damage, anisotropy, and the interpretation of zircon (U-Th)/He thermochronology. American Journal of Science, 313(3), 145–198. https://doi. org/10.2475/03.2013.01
- Guenthner, W. R., Reiners, P. W., & Tian, Y. (2014). Interpreting date-eU correlations in zircon (U-Th)/He data sets: A case study from the Longmen Shan, China. Earth and Planetary Science Letters, 403, 328–339. https://doi.org/10.1016/j.epsl.2014.06.050
- Guo, X. Y., Gao, R., Zhao, J. M., Xu, X., Lu, Z. W., Klemperer, S. L., & Liu, H. (2018). Deep-seated lithospheric geometry in revealing collapse of the Tibetan Plateau. *Earth-Science Reviews*, 185, 751–762. https://doi.org/10.1016/j.earscirev.2018.07.013
- Guo, Z., Gao, X., Yao, H., Li, J., & Wang, W. (2009). Midcrustal low-velocity layer beneath the central Himalaya and southern Tibet revealed by ambient noise array tomography. *Geochemistry, Geophysics, Geosystems*, 10(5). https://doi.org/10.1029/2009GC002458
- Guo, Z. F., & Wilson, M. (2019). Late Oligocene-early Miocene transformation of postcollisional magmatism in Tibet. Geology, 47, 776–780. https://doi.org/10.1130/G46147.1
- Guo, Z. F., Wilson, M., Zhang, M. L., Cheng, Z. H., & Zhang, L. H. (2013). Post-collisional, K-rich mafic magmatism in South Tibet: Constraints on Indian slab-to-wedge transport processes and plateau uplift. Contributions to Mineralogy and Petrology, 165(6), 1311–1340. https://doi. org/10.1007/s00410-013-0860-y
- Guo, Z. F., Wilson, M., Zhang, M. L., Cheng, Z. H., & Zhang, L. H. (2015). Post-collisional ultrapotassic mafic magmatism in South Tibet: Products of partial melting of pyroxenite in the mantle wedge induced by roll-back and delamination of the subducted Indian continental lithosphere slab. *Journal of Petrology*, 56(7), 1365–1406. https://doi.org/10.1093/petrology/egv040
- Gutscher, M., Dominguez, S., De Lepinay, B. M., Pinheiro, L., Gallais, F., Babonneau, N., et al. (2016). Tectonic expression of an active slab tear from high-resolution seismic and bathymetric data offshore sicily (Ionian sea). *Tectonics*, 35, 39–54. https://doi.org/10.1002/2015TC003898
- Ha, G. H., Wu, Z. H., & Liu, F. (2019). Late quaternary vertical slip rates along the southern Yadong-Gulu rift, Southern Tibetan Plateau. Tectonophysics, 755, 75–90. https://doi.org/10.1016/j.tecto.2019.02.014
- Ha, G. H., Wu, Z. H., & Liu, H. (2018). Late Cenozoic sedimentary strata of Qingduojiang graben, South Tibet: Preliminary constraint on the initial rifting age of SN-trending rift. Acta Geological Sinica, 92(10), 2051–2067. https://doi.org/10.1111/1755-6724.13586
- Hager, C., Stockli, D. F., Dewane, T. J., Gehrels, G., & Ding, L. (2009). Anatomy and crustal evolution of the central Lhasa terrane (S-Tibet) revealed by investigations in the Xainza rift. Geophysical Research Abstracts, EGU General Assembly, 11, 11346–11341.

BIAN ET AL. 19 of 23



- Haproff, P. J., Odlum, M. L., Zuza, A. V., Yin, A., & Stockli, D. F. (2020). Structural and thermochronologic constraints on the Cenozoic tectonic development of the Northern Indo-Burma ranges. *Tectonics*, 39(9), e2020TC006231. https://doi.org/10.1029/2020TC006231
- Haproff, P. J., Zuza, A. V., & Yin, A. (2018). West-directed thrusting south of the Eastern Himalayan syntaxis indicates clockwise crustal flow at the indenter corner during the India-Asia collision. *Tectonophysics*, 722, 277–285. https://doi.org/10.1016/j.tecto.2017.11.001
- Harrison, T. M., Copeland, P., Kidd, W. S. F., & Lovera, O. M. (1995). Activation of the Nyainqentanghla shear zone: Implications for uplift of the southern Tibetan Plateau. *Tectonics*, 14, 658–676. https://doi.org/10.1029/95tc00608
- Herman, F., Copeland, P., Avouac, J. P., Bollinger, L., Mahéo, G., Le Fort, P. L., et al. (2010). Exhumation, crustal deformation, and thermal structure of the Nepal Himalaya derived from the inversion of thermochronological and thermobarometric data and modeling of the topography. Journal of Geophysical Research: Solid Earth, 115(B6), 25–39. https://doi.org/10.1029/2008jb006126
- Hintersberger, E., Thiede, R. C., Strecker, M. R., & Hacker, B. R. (2010). East-west extension in the NW Indian Himalaya. *The Geological Society of America Bulletin*, 122, 1499–1515. https://doi.org/10.1130/B26589.1
- Hoke, L., Lamb, S., Hilton, D. R., & Poreda, R. J. (2000). Southern limit of mantle-derived geothermal helium emissions in Tibet: Implications for lithospheric structure. Earth and Planetary Science Letters, 180(3-4), 297-308. https://doi.org/10.1016/S0012-821X(00)00174-6
- Hou, Z. Q., Zhang, Z. D., Gao, Y. F., Yang, Z. M., & Jiang, W. (2006). Tearing and dischronal subduction of the Indian continental slab: Evidence from Cenozoic Gangdese volcano-magmatic rocks in South Tibet. Acta Petrologica Sinica, 22, 761–774. (in Chinese with English abstract).
- Hu, J., & Liu, L. (2016). Abnormal seismological and magmatic processes controlled by the tearing South American flat slabs. Earth and Planetary Science Letters, 450, 40–51. https://doi.org/10.1016/j.epsl.2016.06.019
- Hurford, A. J., & Green, P. F. (1983). The zeta age calibration of fission-track dating. Chemical Geology, 41, 285–317. https://doi.org/10.1016/ S0009-2541(83)80026-6
- Johnson, J. E., Flowers, R. M., Baird, G. B., & Mahan, K. H. (2017). "Inverted" zircon and apatite (U-Th)/He dates from the front range, Colorado: High-damage zircon as a low-temperature (<50°C) thermochronometer. Earth and Planetary Science Letters, 466, 80–90. https://doi.org/10.1016/j.epsl.2017.03.002</p>
- Kali, E., Leloup, P. H., Arnaud, N., Maheo, G., Liu, D. Y., Boutonnet, E., et al. (2010). Exhumation history of the deepest central Himalayan rocks Ama Drime range: Key pressure-temperature-deformation-time constraints on orogenic models. *Tectonics*, 29, TC2014. https://doi. org/10.1029/2009TC002551
- Kapp, J. L. D., Harrison, T. M., Kapp, P., Grove, M., Lovera, O. M., & Ding, L. (2005). Nyainqentanglha Shan: A window into the tectonic, thermal, and geochemical evolution of the Lhasa block, southern Tibet. *Journal of Geophysical Research: Solid Earth*, 110, 653–669. https://doi.org/10.1029/2004JB003330
- Kapp, P., & Guynn, J. H. (2004). Indian punch rifts Tibet. Geology, 32(11), 993–996. https://doi.org/10.1130/G20689.1
- Kapp, P., Taylor, M., Stockli, D., & Ding, L. (2008). Development of active low-angle normal fault systems during orogenic collapse: Insight from Tibet. Geology, 36(1), 7–10. https://doi.org/10.1130/G24054A.1
- Ketcham, R. A., Gautheron, C., & Tassan-Got, L. (2011). Accounting for long alpha-particle stopping distances in (U-Th-Sm)/He geochronology: Refinement of the baseline case. *Geochimica et Cosmochimica Acta*, 75(24), 7779–7791. https://doi.org/10.1016/j.gca.2011.10.011
- Kind, R., & Yuan, X. H. (2010). Seismic images of the biggest crash on Earth. Science, 329(5998), 1479–1480. https://doi.org/10.1126/science.1191620
- King, G. E., Herman, F., & Guralnik, B. (2016). Northward migration of the Eastern Himalayan syntaxis revealed by OSL thermochronometry. Science, 353(6301), 800–804. https://doi.org/10.1126/science.aaf2637
- Klootwijk, C. T., Conaghan, P. J., & Powell, C. M. (1985). The Himalayan arc: Large-scale continental subduction, oroclinal bending and back-arc spreading. Earth and Planetary Science Letters, 75(2–3), 167–183. https://doi.org/10.1016/0012-821X(85)90099-8
- Kosarev, G., Kind, R., Sobolev, S. V., Yuan, X. H., Hanka, W., & Oreshin, S. (1999). Seismic evidence for a detached India lithospheric mantle beneath Tibet. *Science*, 283, 1306–1309. https://doi.org/10.1126/science.283.5406.1306
- Koulakov, I., Kasatkina, E., Shapiro, N. M., Jaupart, C., Vasilevsky, A., Khrepy, S. E., et al. (2016). The feeder system of the Toba supervolcano from the slab to the shallow reservoir. *Nature Communications*, 7, 12228. https://doi.org/10.1038/ncomms12228
- Langille, J. M., Jessup, M. J., Cottle, J. M., Lederer, G., & Ahmad, T. (2012). Timing of metamorphism, melting and exhumation of the Leo Pargil dome, northwest India. *Journal of Metamorphic Geology*, 30(8), 769–791. https://doi.org/10.1111/j.1525-1314.2012.00998.x
- Larson, K. P., Kellett, D. A., Cottle, J. M., Camacho, A., & Brubacher, A. D. (2020). Mid-Miocene initiation of E-W extension and recoupling of the Himalaya. Terra Nova, 32(2), 151–158. https://doi.org/10.1111/ter.12443
- Laskowski, A. K., Kapp, P., Ding, L., Campbell, C., & Liu, X. H. (2017). Tectonic evolution of the Yarlung suture zone, Lopu Range region, southern Tibet. *Tectonics*, 36, 108–136. https://doi.org/10.1002/2016tc004334
- Leary, R., Orme, D. A., Laskowski, A. K., Decelles, P. G., Kapp, P., Carrapa, B., & Dettinger, M. (2016). Along-strike diachroneity in deposition of the Kailas Formation in central southern Tibet: Implications for Indian slab dynamics. *Geosphere*, 12(4), 1–1223. https://doi.org/10.1130/GES01325.1
- Lechmann, S. M., Schmalholz, S. M., Hetényi, G., May, D. A., & Kaus, B. J. P. (2014). Quantifying the impact of mechanical layering and under-thrusting on the dynamics of the modern India-Asia collisional system with 3-D numerical models. *Journal of Geophysical Research: Solid Earth*, 119, 1–644. https://doi.org/10.1002/2012JB009748
- Lee, J., Hager, C., Wallis, S. R., Stockli, D. F., Whitehouse, M. J., Aoya, M., & Wang, Y. (2011). Middle to late Miocene extremely rapid exhumation and thermal reequilibration in the Kung Co rift, southern Tibet. *Tectonics*, 30(2), TC2007. https://doi.org/10.1029/2010TC002745
- Li, C., Hilst, R. D. V. D., Meltzer, A. S., & Engdahl, E. R. (2008). Subduction of the Indian lithosphere beneath the Tibetan Plateau and Burma. Earth and Planetary Science Letters, 274, 157–168. https://doi.org/10.1016/j.epsl.2008.07.016
- Li, J. T., & Song, X. D. (2018). Tearing of Indian mantle lithosphere from high-resolution seismic images and its implications for lithosphere deformation in southern Tibet. Proceedings of the National Academy of sciences of the United States of America, 115, 8296–8300. https://doi. org/10.1073/pnas.1717258115
- Li, L., Murphy, M. A., & Gao, R. (2020). Subduction of the Indian plate and the nature of the crust beneath western Tibet: Insights from seismic imaging. *Journal of Geophysical Research: Solid Earth*, 125, e2020JB019684. https://doi.org/10.1029/2020JB019684
- Li, S. H., van Hinsbergen, D. J. J., Najman, Y., Jing, L.-Z., Deng, C. L., & Zhu, R. X. (2020). Does pulsed Tibetan deformation correlate with Indian plate motion changes? *Earth and Planetary Sciences Letters*, 536, 116144. https://doi.org/10.1016/j.epsl.2020.116144
- Li, Z. H., Xu, Z., Gerya, T., & Burg, J. P. (2013). Collision of continental corner from 3-D numerical modeling. Earth and Planetary Science Letters, 380, 98–111. https://doi.org/10.1016/j.epsl.2013.08.034
- Liang, X. F., Chen, Y., Tian, X. B., Chen, Y. J., Ni, J., Gallegos, A., et al. (2016). 3-D imaging of subducting and fragmenting Indian continental lithosphere beneath southern and central Tibet using body-wave finite-frequency tomography. *Earth and Planetary Science Letters*, 443, 162–175. https://doi.org/10.1016/j.epsl.2016.03.029

BIAN ET AL. 20 of 23



- Liao, J., & Gerya, T. V. (2014). Influence of lithospheric mantle stratification on craton extension: Insight from two-dimensional thermo-mechanical modeling. *Tectonophysics*, 631, 50–64. https://doi.org/10.1016/j.tecto.2014.01.020
- Lin, C., Zhang, J. J., Wang, X. X., Huang, T. L., Zhang, B., & Fan, Y. S. (2021). Himalayan Miocene adaktic rocks, a case study of the Mayum pluton: Insights into geodynamic processes within the subducted Indian continental lithosphere and Himalayan mid-Miocene tectonic regime transition. The Geological Society of America Bulletin, 133(3-4), 591–611. https://doi.org/10.1130/B35640.1
- Liu, M., & Yang, Y. (2003). Extensional collapse of the Tibetan Plateau: Results of three-dimensional finite element modeling. *Journal of Geophysical Research: Solid Earth*, 108(B8), 2361. https://doi.org/10.1029/2002jb002248
- Liu, Z., Tian, X. B., Yuan, X. H., Liang, X. F., Chen, Y., Zhu, G. H., et al. (2020). Complex structure of upper mantle beneath the Yadong-Gulu rift in Tibet revealed by S-to-P converted waves. Earth and Planetary Science Letters, 531, 115954. https://doi.org/10.1016/j.epsl.2019.115954
- Liu, Z. C., Wu, F. Y., Qiu, Z. L., Wang, J. G., Liu, X. C., Ji, W. Q., & Liu, C.-Z. (2017). Leucogranite geochronological constraints on the termination of the South Tibetan Detachment in Eastern Himalaya. *Tectonophysics*, 721, 106–122. https://doi.org/10.1016/j.tecto.2017.08.019
- Lu, T. Y., He, Z. Y., & Klemd, R. (2020). Two phases of post-onset collision adaktic magmatism in the southern Lhasa subterrane, Tibet, and their tectonic implications. The Geological Society of America Bulletin, 132(7–8), 1587–1602. https://doi.org/10.1130/B35326.1
- Mahéo, G., Leloup, P. H., Valli, F., Lacassin, R., Arnaud, N., Paquette, J. L., et al. (2007). Post 4 Ma initiation of normal faulting in southern Tibet. Constraints from the Kung Co half graben. Earth and Planetary Science Letters, 256, 233–243. https://doi.org/10.1016/j.epsl.2007.01.029
- Manighetti, I., Caulet, C., Barros, L. D., Perrin, C., Cappa, F., & Gaudemer, Y. (2015). Generic along-strike segmentation of Afar normal faults, East Africa: Implications on fault growth and stress heterogeneity on seismogenic fault planes. *Geochemistry, Geophysics, Geosystems*, 16(2), 443–467. https://doi.org/10.1002/2014GC005691
- McCaffrey, R., & Nabelek, J. (1998). Role of oblique convergence in the active deformation of the Himalayas and southern Tibet plateau. *Geology*, 26, 691–694. https://doi.org/10.1130/0091-7613(1998)026<0691:ROOCIT>2.3.CO;2
- McCallister, A. T., Taylor, M. H., Murphy, M. A., Styron, R. H., & Stockli, D. F. (2014). Thermochronologic constraints on the late Cenozoic exhumation history of the Gurla Mandhata metamorphic core complex, Southwestern Tibet. *Tectonics*, 33, 27–52. https://doi.org/10.1002/2013TC003302
- McDougall, L., & Harrison, T. M. (1999). Geochronology and thermochronology by the <sup>40</sup>Ar/<sup>39</sup>Ar method (2nd ed.). New York: Oxford University Press.
- Miller, M. S., Gorbatov, A., & Kennett, B. (2006). Three-dimensional visualization of a near-vertical slab tear beneath the southern mariana arc. Geochemistry, Geophysics, Geosystems, 7(6), Q06012. https://doi.org/10.1029/2005GC001110
- Molnar, P., & Lyon-Caent, H. (1989). Fault plane solutions of earthquakes and active tectonics of the Tibetan Plateau and its margins. *Geophysical Journal International*, 99(1), 123–154. https://doi.org/10.1111/j.1365-246X.1989.tb02020.x
- Molnar, P., & Tapponnier, P. (1978). Active tectonics of Tibet. Journal of Geophysical Research: Solid Earth, 83(B11), 5361–5375. https://doi.org/10.1029/jb083jb11p05361
- Murphy, M. A., & Copeland, P. (2005). Transtensional deformation in the central Himalaya and its role in accommodating growth of the Himalayan orogen. *Tectonics*, 24(4), TC4012. https://doi.org/10.1029/2004TC001659
- Murphy, M. A., Saylor, J. E., & Ding, L. (2009). Late Miocene topographic inversion in southwest Tibet based on integrated paleoelevation reconstructions and structural history. Earth and Planetary Science Letters, 282(1–4), 1–9. https://doi.org/10.1016/j.epsl.2009.01.006
- Murphy, M. A., Yin, A., Kapp, P., Harrison, T. M., Manning, C. E., Ryerson, F. J., et al. (2002). Structural evolution of the Gurla Mandhata detachment system, southwest Tibet: Implications for the eastward extent of the Karakoram fault system. *The Geological Society of America Bulletin*, 114, 428–447. https://doi.org/10.1130/0016-7606(2002)114<0428:seotgm>2.0.co;2
- Nabelek, J., Hetenyi, G., Vergne, J., Sapkota, S., Kafle, B., Jiang, M., et al. (2009). Underplating in the Himalaya-Tibet collision zone revealed by the Hi-CLIMB experiment. *Science*, 325, 1371–1374. https://doi.org/10.1126/science.1167719
- Nie, S. T., Tian, X. B., Liang, X. F., Chen, Y., & Xu, T. (2020). Pn uppermost mantle tomography of central Tibet: Implication for mechanisms of NS rifts and conjugate faults. *Tectonophysics*, 788, 228499. https://doi.org/10.1016/j.tecto.2020.228499
- Obayashi, M., Yoshimitsu, J., & Fukao, Y. (2009). Tearing of stagnant slab. Science, 324, 1173–1175. https://doi.org/10.1126/science.1172496
  Pang, Y. J., Zhang, H., Gerya, T. V., Liao, J., Cheng, H. H., & Shi, Y. L. (2018). The mechanism and dynamics of N-S rifting in southern Tibet: Insight from 3-D thermomechanical modeling. Journal of Geophysical Research: Solid Earth, 123(B14), 859–877. https://doi.org/10.1002/2017JB014011
- Pei, S. P., Liu, H. B., Bai, L., Liu, Y. B., & Sun, Q. (2016). High-resolution seismic tomography of the 2015 M<sub>w</sub>7.8 Gorkha earthquake, Nepal: Evidence for the crustal tearing of the Himalayan rift. *Geophysical Research Letters*, 43, 9045–9052. https://doi.org/10.1002/2016GL069808
- Priestley, K., Debayle, E., McKenzie, D., & Pilidou, S. (2006). Upper mantle structure of eastern Asia from multimode surface waveform tomography. Journal of Geophysical Research: Solid Earth, 111, B10304. https://doi.org/10.1029/2005JB004082
- Ratschbacher, L., Krumrei, I., Blumenwitz, M., Staiger, M., Gloaguen, R., Miller, B. V., et al. (2011). Rifting and strike-slip shear in central Tibet and the geometry, age and kinematics of upper crustal extension in Tibet. *Geological Society, London, Special Publications*, 353(1), 127–163. https://doi.org/10.1144/SP353.8
- Ren, Y., & Shen, Y. (2008). Finite frequency tomography in southeastern Tibet: Evidence for the causal relationship between mantle lith-osphere delamination and the north-south trending rifts. *Journal of Geophysical Research: Solid Earth*, 113, B10316. https://doi.org/10.1029/2008JB005615
- Replumaz, A., Negredo, A. M., Villaseñor, A., & Guillotet, S. (2010). Indian continental subduction and slab break-off during Tertiary collision. Terra Nova, 22(4), 290–no. https://doi.org/10.1111/j.1365-3121.2010.00945.x
- Royden, L., Patacca, E., & Scandone, P. (1987). Segmentation and configuration of subducted lithosphere in Italy: An important control on thrust-belt and foredeep-basin evolution. Geology, 15, 714–717. https://doi.org/10.1130/0091-7613(1987)15
- Sambridge, M. (1999a). Geophysical inversion with a neighbourhood algorithm-I. Searching a parameter space. Geophysical Journal of the Royal Astronomical Society, 138(2), 479–494. https://doi.org/10.1046/j.1365-246X.1999.00876.x
- Sambridge, M. (1999b). Geophysical inversion with a neighbourhood algorithm-II. Appraising the ensemble. Geophysical Journal of the Royal Astronomical Society, 138(3), 727–746. https://doi.org/10.1046/j.1365-246x.1999.00900.x
- Sanchez, V. I., Murphy, M. A. R., Robinson, A. C., Lapen, T. J., Heizler, M. T., & Taylor, M. H. (2010). Onset of oblique extension in south-central Tibet by 15 Ma: Implications for diachronous extension of the Tibetan Plateau. San Francisco: American Geophysical Union.
- Saylor, J. E., De Celles, P. G., & Quade, J. (2010). Climate-driven environmental change in the Zhada basin, southwestern Tibet Plateau. Geosphere, 6, 74–92. https://doi.org/10.1130/ges00507.1
- Saylor, J. E., Quade, J., Dellman, D. L., DeCelles, P. G., Kapp, P. A., & Ding, L. (2009). The late Miocene through present paleoelevation history of southwestern Tibet. *American Journal of Science*, 309, 1–42. https://doi.org/10.2475/01.2009.01
- Schwarz, G. (1978). Estimating the dimension of a model. Annals of Statistics, 6(2), 461-464. https://doi.org/10.1214/aos/1176344136

BIAN ET AL. 21 of 23



- Seeber, L., & Armbruster, J. G. (1984). Some elements of continental subduction along the Himalayan front. *Tectonophysics*, 105, 263–278. https://doi.org/10.1016/0040-1951(84)90207-5
- Seeber, L., & Pêcher, A. (1998). Strain partitioning along the Himalayan arc and the Nanga Parbat antiform. Geology, 26, 791–794. https://doi.org/10.1130/0091-7613(1998)026<0791:SPATHA>2.3.CO;2
- Shen, T. Y., Wang, G. C., Leloup, P. H., van der Beek, P., Bernet, M., Cao, K., et al. (2016). Controls on Cenozoic exhumation of the Tethyan Himalaya from fission-track thermochronology and detrital zircon U-Pb geochronology in the Gyirong basin area, southern Tibet. *Tectonics*, 35(7), 1713–1734. https://doi.org/10.1002/2016TC004149
- Shi, D. N., Wu, Z. J., Klemperer, S. L., Zhao, W. J., Xue, G. Q., & Su, H. P. (2015). Receiver function imaging of crustal suture, steep subduction, and mantle wedge in the eastern India-Tibet continental collision zone. Earth and Planetary Science Letters, 414, 6–15. https://doi.org/10.1016/j.epsl.2014.12.055
- Shi, D. N., Zhao, W. J., Klemperer, S. L., Wu, Z. J., Mechie, J., Shi, J. Y., et al. (2016). West-east transition from underplating to steep subduction in the India-Tibet collision zone revealed by receiver-function profiles. *Earth and Planetary Science Letters*, 452, 171–177. https://doi.org/10.1016/j.epsl.2016.07.051
- Si, S. K., Gao, R., & Tian, X. B. (2019). East-west differential underthrusting of the Indian lithospheric plate beneath central Tibet revealed by imaging V<sub>p</sub>/V<sub>s</sub>. Journal of Geophysical Research: Solid Earth, 124, 9714–9730. https://doi.org/10.1029/2018JB017259
- Spakman, W., & Hall, R. (2010). Surface deformation and slab-mantle interaction during Banda arc subduction rollback. Nature Geoscience, 3(8), 562–566. https://doi.org/10.1038/NGE0917
- Sternai, P., Jolivet, L., Menant, A., & Gerya, T. (2014). Driving the upper plate surface deformation by slab rollback and mantle flow. Earth and Planetary Science Letters, 405, 110–118. https://doi.org/10.1016/j.epsl.2014.08.023
- Stockli, D., Taylor, M., Yin, A., Harrison, T. M., D'Andrea, J., Kapp, P., et al. (2002). Late Miocene-Pliocene inception of E-W extension in Tibet as evidenced by apatite (U-Th)/He data. Geological Society of America, Abstracts with Programs, 34, 411.
- Styron, R. H., Taylor, M., & Sundell, K. (2015). Accelerated extension of Tibet linked to the northward underthrusting of Indian crust. *Nature Geoscience*, 8, 131–134. https://doi.org/10.1038/ngeo2336
- Styron, R. H., Taylor, M. H., & Murphy, M. A. (2011). Oblique convergence, arc-parallel extension, and the role of strike-slip faulting in the High Himalaya. *Geosphere*, 7(2), 582–596. https://doi.org/10.1130/GES00606.1
- Styron, R. H., Taylor, M. H., Sundell, K. E., Stockli, D. F., Oalmann, J. A. G., Möller, A., et al. (2013). Miocene initiation and acceleration of extension in the South Lunggar rift, western Tibet: Evolution of an active detachment system from structural mapping and (U-Th)/He thermochronology. *Tectonics*, 32(4), 880. https://doi.org/10.1002/tect.20053
- Sundell, K. E., Laskowski, A. K., Kapp, P. A., Ducea, M. N., & Chapman, J. B. (2021). Jurassic to Neogene quantitative crustal thickness estimates in southern Tibet. Geological Society of America Today, 31. https://doi.org/10.1130/GSATG461A.1
- Sundell, K. E., Taylor, M. H., Styron, R. H., Stockli, D. F., Kapp, P., Hager, C., et al. (2013). Evidence for constriction and Pliocene acceleration of east-west extension in the North Lunggar rift region of west central Tibet. *Tectonics*, 32(5), 1454–1479. https://doi.org/10.1002/tect.20086
- Taylor, M., & Yin, A. (2009). Active structures of the Himalayan-Tibetan orogen and their relationships to earthquake distribution, contemporary strain field, and Cenozoic volcanism. *Geosphere*, 5(3), 199–214. https://doi.org/10.1130/GES00217.1
- Thiede, R. C., Arrowsmith, J. R., Bookhagen, B., McWilliams, M., Sobel, E. R., & Strecker, M. R. (2006). Dome formation and extension in the Tethyan Himalaya, Leo Pargil, northwest India. *The Geological Society of America Bulletin*, 118(5–6), 635–650. https://doi.org/10.1130/ B25872.1
- Tian, X. B., Chen, Y., Tseng, T. L., Klemperer, S. L., Thybo, H., Liu, Z., et al. (2015). Weakly coupled lithospheric extension in southern Tibet. Earth and Planetary Science Letters, 430, 171–177, https://doi.org/10.1016/j.epsl.2015.08.025
- Tremblay, M. M., Fox, M., Schmidt, J. L., Tripathy-Lang, A., Wielicki, M. M., Harrison, T. M., et al. (2015). Erosion in southern Tibet shut down at ~10 Ma due to enhanced rock uplift within the Himalaya. *Proceedings of the National Academy of sciences of the United States of America*, 112, 12030–12035. https://doi.org/10.1073/pnas.1515652112
- Valla, P. G., Herman, F., van der Beek, P. A., & Braun, J. (2010). Inversion of thermochrono-logical age-elevation profiles to extract independent estimates of denudation and relief history—I: Theory and conceptual model. *Earth and Planetary Science Letters*, 295, 511–522. https://doi.org/10.1016/j.epsl.2010.04.033
- van der Beek, P. A., Valla, P. G., Herman, F., Braun, J., Persano, C., Dobson, K. J., & Labrin, E. (2010). Inversion of thermochronological age-elevation profiles to extract independent estimates of denudation and relief history—II: Application to the French Western Alps. *Earth and Planetary Science Letters*, 296(1–2), 9–22. https://doi.org/10.1016/j.epsl.2010.04.032
- Voronoi, G. (1909). Nouvelles applications des paramètres continus à théorie des formes quadratiques. Deuxième Mémoire. Recherches sur les paralléloèdres primitifs. *Journal für die Reine und Angewandte Mathematik*, 134, 198–287. https://doi.org/10.1515/crll.1909.136.67
- Wang, A., Min, K., Wang, G. C., Cao, K., Shen, T. Y., Jiang, P. F., & Wei, J. (2019). Slow exhumation of the Greater Himalaya in the Yadong region, the transition between the Central and Eastern Himalaya, during the late Neogene. *Journal of the Geological Society*, 176, 1207–1217. https://doi.org/10.1144/jgs2018-186
- Wang, G., Wei, W. B., Ye, G. F., Jin, S., Jing, J., Zhang, L. T., et al. (2017). 3-D electrical structure across the Yadong-Gulu rift revealed by magnetotelluric data: New insights on the extension of the upper crust and the geometry of the underthrusting Indian lithospheric slab in southern Tibet. Earth and Planetary Science Letters, 474, 172–179. https://doi.org/10.1016/j.epsl.2017.06.027
- Wang, M., & Shen, Z. K. (2020). Present-day crustal deformation of continental China derived from GPS and its tectonic implications. *Journal of Geophysical Research: Solid Earth*, 125, e2019JB018774. https://doi.org/10.1029/2019JB018774
- Wang, Q., Zhang, P. Z., Freymueller, J. T., Bilham, R., Larson, K. M., Lai, X., et al. (2001). Present-day crustal deformation in China constrained by Global Positioning System measurements. *Science*, 294(5542), 574–577. https://doi.org/10.1126/science.1063647
- Wang, R., Richards, J. P., Zhou, L. M., Hou, Z. Q., Stern, R. A., Creaser, R. A., & Zhu, J.-j. (2015). The role of Indian and Tibetan lithosphere in spatial distribution of Cenozoic magmatism and porphyry Cu–Mo deposits in the Gangdese belt, southern Tibet. Earth-Science Reviews, 150, 68–94. https://doi.org/10.1016/j.earscirev.2015.07.003
- Wang, R., Weinberg, R. F., Zhu, D. C., Hou, Z. Q., & Yang, Z. M. (2021). The impact of a tear in the subducted Indian plate on the Miocene geology of the Himalayan-Tibetan orogen. *The Geological Society of America Bulletin*, 134, 681–690. https://doi.org/10.1130/B36023.1
- Wang, S. G., Chevalier, M. L., Pan, J. W., Bai, M. K., Li, K. Y., Li, H. B., & Wang, G. (2020). Quantification of the late Quaternary throw rates along the Yadong rift, southern Tibet. *Tectonophysics*, 790, 228545. https://doi.org/10.1016/j.tecto.2020.228545
- Webb, A. A. D., Guo, H., Clift, P. D., Husson, L., Müller, T., Costantino, D., et al. (2017). The Himalaya in 3-D: Slab dynamics controlled mountain building and monsoon intensification. *Lithosphere*, 9(4), 637–651. https://doi.org/10.1130/L636.1
- Williams, H., Turner, S., Kelley, S., & Harris, N. (2001). Age and composition of dikes in Southern Tibet: New constraints on the timing of east-west extension and its relationship to postcollisional volcanism. *Geology*, 29(4), 339–342. https://doi.org/10.1130/0091-7613(2001)029 <0339:AACODI>2.0.CO;2

BIAN ET AL. 22 of 23



- Wolf, R. A., Farley, K. A., & Silver, L. T. (1996). Helium diffusion and low-temperature thermochronometry of apatite. *Geochimica et Cosmochimica Acta*, 60(21), 4231–4240. https://doi.org/10.1016/S0016-7037(96)00192-5
- Wolff, R., Hetzel, R., Dunkl, I., Anczkiewicz, A. A., & Pomella, H. (2020). Fast cooling of normal-fault footwalls: Rapid fault slip or thermal relaxation? *Geology*, 48(4), 333–337. https://doi.org/10.1130/G46940.1
- Wolff, R., Hetzel, R., Dunkl, I., Xu, Q., Bröcker, M., & Anczkiewicz, A. A. (2019). High-angle normal faulting at the Tangra Yumco graben (southern Tibet) since ∼15 Ma. *The Journal of Geology*, 127, 15–36. https://doi.org/10.1086/700406
- Woodruff, W. H., Horton, B. K., Kapp, P., & Stockli, D. F. (2013). Late Cenozoic evolution of the Lunggar extensional basin, Tibet: Implications for basin growth and exhumation in hinterland plateaus. *The Geological Society of America Bulletin*, 125(3/4), 343–358. https://doi.org/10.1130/B30664.1
- Wu, C. D., Nelson, K. D., Wortman, G., Samson, S. D., Yue, Y., Li, J., et al. (1998). Yadong cross structure and South Tibetan Detachment in the east central Himalaya (89°–90°E). *Tectonics*, 17(1), 28–45. https://doi.org/10.1029/97TC03386
- Wu, C. L., Tian, X. B., Xu, T., Liang, X. F., Chen, Y., Taylor, M., et al. (2019). Deformation of crust and upper mantle in central Tibet caused by the northward subduction and slab tearing of the Indian lithosphere: New evidence based on shear wave splitting measurements. *Earth and Planetary Science Letters*, 514, 75–83. https://doi.org/10.1016/j.epsl.2019.02.037
- Wu, Z. H., Ye, P. S., Wang, C. M., Zhang, K. Q., Zhao, H., Zheng, Y. G., et al. (2015). The relics, ages and significance of prehistoric large earthquakes in the Angang graben in South Tibet. Earth Science—Journal of China University of Geosciences, 40(10), 1621. (in Chinese with English abstract). https://doi.org/10.3799/dqkx.2015.147
- Wu, Z. H., Zhao, X., Wu, Z. H., Jiang, W., Hu, D. G., & Zhou, C. (2004). Quaternary geology and faulting in the Damxung-Yangbajain basin. Acta Geologica Sinica, 78(1), 273–282.
- Xiao, L., Wang, C. Z., & Pirajno, F. (2007). Is the underthrust India lithosphere split beneath the Tibetan Plateau? *International Geology Review*, 49, 90–98. https://doi.org/10.2747/0020-6814.49.1.90
- Xu, Z. Q., Wang, Q., Pêcher, A., Liang, F. H., Qi, X. X., Cai, Z. H., et al. (2013). Orogen-parallel ductile extension and extrusion of the Greater Himalaya in the late Oligocene and Miocene. *Tectonics*, 32, 191–215. https://doi.org/10.1002/tect.20021
- Yan, H. Y., Long, X. P., Li, J., Wang, Q., Wang, X. C., Wu, B., et al. (2019). Miocene adakites in South Tibet: Partial melting of the thickened Lhasa juvenile mafic lower crust with the involvement of ancient Indian continental crust compositions. *The Geological Society of America Bulletin*, 132(5–6), 1273–1290. https://doi.org/10.1130/B35239.1
- Yang, G., Tang, Y., Lei, D. N., Hu, Q., & Wu, J. C. (2020). Holocene activity and seismic hazard analysis of faults in Damxung, Tibet. Acta Geophysica, 68, 597–604. https://doi.org/10.1007/s11600-020-00426-z
- Yang, Y. Q., & Liu, M. (2013). The Indo-Asian continental collision: A 3-D viscous model. Tectonophysics, 606, 198–211. https://doi.org/10.1016/j.tecto.2013.06.032
- Yin, A. (2000). Mode of Cenozoic east-west extension in Tibet suggests a common origin of rifts in Asia during Indo-Asian collision. *Journal of Geophysical Research*: Solid Earth. 105(B9), 21745–21759. https://doi.org/10.1029/2000JB900168
- Yin, A. (2006). Cenozoic tectonic evolution of the Himalayan orogen as constrained by along-strike variation of structural geometry, exhumation history, and foreland sedimentation. *Earth-Science Reviews*, 76(1–2), 1–131. https://doi.org/10.1016/j.earscirev.2005.05.004
- Yin, A., & Taylor, M. H. (2011). Mechanics of V-shaped conjugate strike-slip faults and the corresponding continuum mode of continental deformation. The Geological Society of America Bulletin, 123, 1798–1821. https://doi.org/10.1130/b30159.1
- Zhang, J. J., & Guo, L. (2007). Structure and geochronology of the southern Xainza-Dinggye rift and its relationship to the South Tibetan Detachment system. *Journal of Southeast Asian Earth Sciences*, 29, 722–736. https://doi.org/10.1016/j.jseaes.2006.05.003
- Zhang, L. Y., Ducea, M. N., Ding, L., Pullen, A., Kapp, P., & Hoffman, D. (2014). Southern Tibetan Oligocene-Miocene adakites: A record of Indian slab tearing. *Lithos*, 210–211, 209–223. https://doi.org/10.1016/j.lithos.2014.09.029
- Zhang, Z. J., Chen, Y., Yuan, X. H., Tian, X. B., Klemperer, S. L., Xu, T., et al. (2013). Normal faulting from simple shear rifting in Southern Tibet, using evidence from passive seismic profiling across the Yadong-Gulu Rift. *Tectonophysics*, 606, 178–186. https://doi.org/10.1016/j.
- Zhao, J. M., Yuan, X. H., Liu, H. B., Kumar, P., Pei, S. P., Kind, R., et al. (2010). The boundary between the Indian and Asian tectonic plates below Tibet. *Proceedings of the National Academy of Sciences of the United States of America*, 107, 11229–11233. https://doi.org/10.1073/pnas.1001921107
- Zheng, G., Wang, H., Wright, T. J., Lou, Y. D., Zhang, R., Zhang, W. X., et al. (2017). Crustal deformation in the India-Eurasia collision zone from 25 yr of GPS measurements. *Journal of Geophysical Research: Solid Earth*, 122, 9290–9312. https://doi.org/10.1002/2017JB014465
- Zhou, H. W., & Murphy, M. A. (2005). Tomographic evidence for wholesale underthrusting of India beneath the entire Tibetan plateau. *Journal of Asian Earth Sciences*, 25(3), 445–457. https://doi.org/10.1016/j.jseaes.2004.04.007
- Zuo, J. M., Wu, Z. H., Ha, G. G., Hu, M. M., Zhou, C. J., & Gai, H. L. (2021). Spatial variation of nearly NS-trending normal faulting in the southern Yadong-Gulu rift, Tibet: New constraints from the Chongba Yumtso fault, Duoqing Co graben. *Journal of Structural Geology*, 144, 104256. https://doi.org/10.1016/j.jsg.2020.10425691

## **References From the Supporting Information**

- Mitsuishi, M., Wallis, S. R., Aoya, M., Lee, J., & Wang, Y. (2012). E-W extension at 19 Ma in the Kung Co area, S. Tibet: Evidence for contemporaneous E-W and N-S extension in the Himalayan orogen. Earth and Planetary Science Letters, 325–326, 10–20. https://doi.org/10.1016/j.epsl.2011.11.013
- Murphy, M. A., Sanchez, V., & Taylor, M. H. (2010). Syncollisional extension along the India-Asia suture zone, south-central Tibet: Implications for crustal deformation of Tibet. Earth and Planetary Science Letters, 290(3–4), 233–243. https://doi.org/10.1016/j.epsl.2009.11.046
- Murphy, M. A., Yin, A., Harrison, T. M., Dürr, S. B., Chen, Z., Ryerson, F. J., et al. (1997). Did the Indo-Asian collision alone create the Tibetan plateau? *Geology*, 25(8), 719–722. https://doi.org/10.1130/0091-7613(1997)025<0719:dtiaca>2.3.co;2
- Sanchez, V. I., Murphy, M. A., Robinson, A. C., Lapen, T. J., & Heizler, M. T. (2013). Tectonic evolution of the India-Asia suture zone since Middle Eocene time, Lopukangri area, south-central Tibet. *Journal of Southeast Asian Earth Sciences*, 62, 205–220. https://doi.org/10.1016/j. jseaes.2012.09.004
- Wu, Z. H., Hu, D. G., Liu, Q. S., Xia, H. D., & Yan, X. L. (2002). The formation and evolution of tectonic landform of Damxung area in central Tibetan Plateau. *Acta Geoscientia Sinica*, 5(23), 423–428.
- Yin, A., Kapp, P. A., Murphy, M. A., Manning, C. E., Harrison, T. M., Grove, M., et al. (1999). Significant late Neogene east-west extension in northern Tibet. *Geology*, 27, 787–790. https://doi.org/10.1130/0091-7613(1999)027<0787:SLNEWE>2.3.CO;2

BIAN ET AL. 23 of 23